OXFORD UNIVERSITY PRESS | Journal of Petrology

Draft Manuscript for Review

Genesis of oceanic oxide gabbros and gabbronorites during reactive melt migration at transform walls (Doldrums Megatransform System; 7-8°N Mid-Atlantic Ridge)

Journal:	*Journal of Petrology*
Manuscript ID	Draft
Manuscript Type:	Original Manuscript
Date Submitted by the Author:	n/a
Complete List of Authors:	Basch, Valentin; Università di Pavia, Dipartimento di Scienze della Terra; CNR-IGG Pavia Skolotnev, Sergey; Geological Institute of the Russian Academy of Science Ferrando, Carlotta; Università di Pavia, Dipartimento di Scienze della Terra Muccini, Filippo; Istituto Nazionale Geofisica e Vulcanologia Palmiotto, Camilla; CNR ISMAR Bologna Peyve, Alexander; Geological Institute of the Russian Academy of Science Ermolaev, Boris; Geological Institute of the Russian Academy of Science Okina, Olga; Geological Institute of the Russian Academy of Science Ligi, Marco; CNR ISMAR Bologna Sanfilippo, Alessio; Università di Pavia, Dipartimento di Scienze della Terra
Keyword:	Lower oceanic crust, Transform faults, Gabbronorites, Oxide gabbros, Lateral differentiation, Melt-rock interaction

Genesis of oceanic oxide gabbros and gabbronorites during reactive melt migration at transform walls (Doldrums Megatransform System; 7-8°N Mid-Atlantic Ridge)

***Basch, V.[1,2], Sanfilippo, A.[1,2], Skolotnev, S.G.[3], Ferrando, C.[1], Muccini, F.[4], Palmiotto, C.[5], Peyve, A.A.[3], Ermolaev, B.V.[3], Okina, O.I.[3], Ligi, M.[5]**

[1] Dipartimento di Scienze della Terra e dell'Ambiente, Università di Pavia, Italy;
valentin.basch@gmail.com; alessio.sanfilippo@unipv.it; ottaferrando@gmail.com
[2] Istituto Geoscienze e Georisorse, Unità di Pavia, CNR, Pavia, Italy
[3] Geological Institute of the Russian Academy of Science, Moscow, Russia
sg_skol@mail.ru; apeyve@yandex.ru; ermolaev-bv@mail.ru; okina@bk.ru
[4] Istituto Nazionale Geofisica e Vulcanologia, Roma, Italy
filippo.muccini@ingv.it
[5] Istituto di Scienze Marine – CNR, Bologna, Italy
camilla.palmiotto@bo.ismar.cnr.it; marco.ligi@bo.ismar.cnr.it

Corresponding author:
* Valentin Basch
valentin.basch@gmail.com
Dipartimento di Scienze della Terra e dell'Ambiente, University of Pavia
Via Ferrata 1, 27100 Pavia, Italy

Abstract:

The Doldrums Megatransform System (~7-8°N, Mid-Atlantic Ridge) shows a complex architecture including four intra-transform ridge segments bounded by five active transform faults. Lower crustal rocks are exposed along the Doldrums and Vernadsky transform walls that bound the northernmost intra-transform ridge segment. The recovered gabbros are characterized by variably evolved chemical compositions, ranging from olivine gabbros to gabbronorites and oxide gabbros, and lack the most primitive gabbroic endmembers (troctolites, dunites). This "excess" in evolved gabbroic lithologies results from melt migration processes involving lateral differentiation at ridge segment edges. Notably, the numerous recovered gabbronorites show up to 20 vol% of coarse-grained orthopyroxene modal contents. Although covariations in mineral and bulk-rock chemical compositions of the olivine and oxide gabbros define trends of crystallization from a common parental melt, the gabbronorites show elevated light over heavy rare earth elements (LREE/HREE) ratios in both bulk-rock and mineral compositions. These features are not consistent with a petrological evolution driven solely by fractional crystallization, which cannot produce the preferential enrichments in highly incompatible elements documented in the orthopyroxene-bearing lithologies. We suggest that gabbronorites crystallized from evolved melts percolating and partly assimilating a pre-existing olivine gabbro matrix. Saturation in orthopyroxene and selective enrichments in LREE relative to M-HREE are both triggered by an increase in assimilated crystal mass, which ranges from negligible in the oxide-gabbros to abundant in the gabbronorites. This melt-rock reaction process has been related to lateral melt migration beneath ridge-transform intersections, where variably evolved melts injected from the peripheral parts of the melting region towards the transform zone may interact with a gabbroic crystal mush to form abundant oxide-bearing gabbronoritic associations.

Keywords: *Lower oceanic crust; Transform faults; Gabbronorites; Oxide gabbros; Lateral differentiation; Melt-rock interaction.*

1. INTRODUCTION

The architecture and composition of the oceanic crust accreted along the ~67000 km of modern oceanic ridges is highly variable (e.g., Chen, 1992; Carbotte and Sheirer, 2004; Cannat *et al.*, 2006, 2019; Dick *et al.*, 2006; White and Klein, 2014) and mainly dependent on the spreading rate and on the temperature of the upwelling mantle (e.g., Parmentier and Phipps Morgan, 1990; Bown and White, 1994; Langmuir and Forsyth, 2007). At slow spreading rates, magmatism is reduced and crustal accretion is partially accommodated by tectonic extension and exhumation of deep material to the seafloor along oceanic detachments or transform faults (e.g., Cann *et al.*, 1997; Buck *et al.*, 2005; Tucholke *et al.*, 2008; Olive and Dublanchet, 2020; Bickert *et al.*, 2021). Between 0°N and 11°N, the Equatorial Atlantic is characterized by large-offset (>500 km) oceanic transform systems that displace the Mid-Atlantic Ridge axis for more than 3000 km in total. Conversely to the classical model of oceanic transform faults, defined as single narrow strike-slip zones offsetting two mid-ocean ridge segments (Wilson, 1965), these large-offset transform domains develop a broad (>100 km) lens-shaped zone of deformation and have been defined as "megatransform systems" (Ligi *et al.*, 2002). Furthermore, some of these equatorial long-offset transform systems are characterized by a multi-fault architecture (i.e., St-Paul and Doldrums megatransforms) and by the formation of magmatically active intra-transform ridges (ITR) developed within a lens-shaped shear zone (e.g., Bonatti, 1978; Sandwell and Smith, 1997; Hekinian *et al.*, 2000; Maia *et al.*, 2019; Skolotnev *et al.*, 2020). The development of ITRs and the active magmatism in these cold systems is thought to result from active mantle upwelling or from transtensive regime resulting from changes in plate motion (Bonatti, 1978; Fox and Gallo, 1984; Maia *et al.*, 2016; Skolotnev *et al.*, 2020).

Independently on the architecture of the megatransform system, their long offset at slow spreading rate results in large age contrast between the ridge axis and the aged lithosphere transposed on the opposite side of the active transform (Hekinian *et al.*, 2000; Ligi *et al.*, 2002, 2005; Maia *et al.*, 2016, 2019; Luo *et al.*, 2021). The juxtaposition of an active ridge axis with such a cold and thick lithosphere may cause a local decrease in the along-axis thermal gradient and degree of mantle melting approaching the transform, a cooling effect referred to as "cold edge effect" (e.g., Klein and Langmuir, 1987; Schilling *et al.*, 1995; Bonatti *et al.*, 1996a,b, 2001; Ligi *et al.*, 2002, 2005; Brunelli *et al.*, 2020).

An increased thickness of the lithosphere impedes shallow mantle melting (e.g., Langmuir & Forsyth, 2007), reduces melt productivity (e.g., Niu, 1997, 2021; Niu and Hekinian, 1997) and may favour interactions between migrating melts and mantle rocks (e.g., Collier and Kelemen, 2010; Dick *et al.*, 2010; Warren and Shimizu, 2010). Notably, dissolution-precipitation reactions occurring in the mantle (e.g., Dijkstra *et al.*, 2003; Suhr *et al.*, 2008; Sanfilippo *et al.*, 2014; Basch *et al.*, 2018, 2019a,

2019b; Rampone *et al.*, 2020) can modify the composition of the percolating melts, leading to specific trace element enrichments and to modifications in the crystallization order and in the liquid and crystal lines of descent (Collier and Kelemen, 2010; Sanfilippo *et al.*, 2016; Basch *et al.*, 2019b). Several studies evidenced that interactions between a melt and a pre-existing matrix may also occur in oceanic magma chambers, with a strong impact on the composition of the newly formed minerals (e.g., Coogan *et al.*, 2000; Lissenberg and Dick, 2008; Lissenberg *et al.*, 2013; Sanfilippo *et al.*, 2020; Ferrando *et al.*, 2021a, 2021b). If a general agreement exists that melt-mush reactions may contribute to the chemical evolution of the lower oceanic crust (Lissenberg and MacLeod, 2016; Lissenberg *et al.*, 2019; Boulanger *et al.*, 2020; Sanfilippo *et al.*, 2020; Ferrando *et al.*, 2021a,b), to what extent these processes may be enhanced by the thickening of the lithosphere, and/or by melt focusing related to the tectonic activity at the transform, is still matter of debate (see Brunelli *et al.*, 2020)

In this contribution, we report bulk-rock and mineral major and trace element compositions of gabbros and associated basalts recovered in the northern part of the Doldrums Megatransform System (7-8°N, Mid-Atlantic Ridge). There, the gabbroic crust sampled at the transform walls is characterized by chemically evolved compositions and shows unexpected occurrence of orthopyroxene as early magmatic phase. We relate these distinct modal and chemical features to the context of long-offset transform domains, and suggest that lateral differentiation, together with melt-mush reactions during melt transport, led to the distinct abundance of oxide gabbros and gabbronorites along transform walls.

2. GEOLOGICAL SETTING

In the Equatorial region of the Atlantic Ocean, the Mid-Atlantic Ridge (MAR) is characterized by short ridge segments (<200 km), separated by long-offset transform faults and megatransform systems, the largest of which are: Romanche (□950 km; e.g., Bonatti *et al.*, 1994; Searle *et al.*, 1994; Ligi *et al.*, 2002); Doldrums (total offset of □630 km; Skolotnev *et al.*, 2020; Sani *et al.*, 2020); St-Paul (total offset of □580 km; e.g., Hekinian *et al.*, 2000) and Vema (□310 km; e.g., Bonatti *et al.*, 2003, 2005; Cipriani *et al.*, 2009; Brunelli *et al.*, 2020). Together, these transform systems offset the Mid-Atlantic Ridge of more than 3000 km (from 16°W to 44°W) between 0°N and 11°N.

The Doldrums transform system is located at 7-8°N in the Equatorial Atlantic and offsets the Mid-Atlantic Ridge by 630 km from 34°W to 39.5°W. Similar to other megatransform systems (e.g., Hekinian *et al.*, 2000; Ligi *et al.*, 2002; Maia *et al.*, 2019), it is characterized by a multi-fault 110 km-wide lens-shaped deformed domain. Recent bathymetric surveys (e.g., Skolotnev *et al.*, 2020) highlighted its morphological complexity, with the occurrence of 4 ITR segments delimited by 5

active transform faults, namely the Doldrums, Vernadsky, 7.4°N, Pushcharovsky and Bogdanov transforms (Fig. 1a). The offsets of the single transform faults increase northwards, reaching 145 km and 177km along the Vernadsky and Doldrums transform faults, respectively. Considering half-spreading rates of 15 mm/yr (Cande *et al.*, 1988), the age offset across these transform faults is □10 Ma and □12 Ma, respectively (Skolotnev *et al.*, 2020).

Dredge sampling along the Doldrums transform system was carried out with *R/V Akademik Nikolaj Strakhov* during two expeditions in the late 1980s' (S06 in 1987-1988 and S09 in 1990; Pushcharovsky *et al.*, 1991, 1992) and more recently in 2019, in the frame of a collaborative Russian-Italian Research Program (S45; Skolotnev *et al.*, 2020). Fifty-two dredges in total recovered exclusively fresh basalts along the ITR-2, ITR-3 and ITR-4, whereas peridotitic and gabbroic rocks were sampled along the Vernadsky and Doldrums transform walls and from bathymetric highs located on the ITR-1 rift shoulders (Fig. 1b; Skolotnev *et al.*, 2020). In this study, we focus on gabbroic rocks and associated basalts sampled in 8 dredge hauls deployed along the two transforms, as reported in Figure 1b.

3. BATHYMETRY AND SAMPLING

The studied samples have all been recovered in the northernmost part of the Doldrums Megatransform System, within the ITR-1 domain. From north to south, the main bathymetric features of the studied area are: *i)* the Doldrums transform valley, *ii)* the ITR-1 segment, *iii)* OCC 8.1°N, *iv)* the Vernadsky transform valley and *v)* Seamount Peyve (Fig. 1).

3.1. Doldrums transform and ITR-1

The Doldrums transform offsets the MAR West and ITR-1 segments by 177 km. Within the Doldrums transform valley, a 130 km-long and 1500 m-high median ridge separates the active transform valley to the south from an inactive transform valley to the north. The median ridge is in continuity with the eastern shoulder of the ITR-1 (Fig. 1b).

The ITR-1 is a 55-kilometre-long ridge segment characterized by a symmetrical rift valley and a continuous axial neovolcanic zone (Supplementary Figure S1a). Although single volcanic edifices can be observed at the northern extremity of the neovolcanic ridge axis, the central part of the rift valley is shallower (4200-4400 metre depth), and the volcanic activity appears more intense.

On the western shoulder of the ITR-1 valley, at the intersection between the ITR-1 and the Doldrums transform valley, a 25 km-long and 20 km-wide inner corner high previously described as an Oceanic Core Complex (OCC 8.1°N; Skolotnev *et al.*, 2020) shows a dome-shaped structure and reaches 1600m depth (Fig. S1a). It is characterized by gentle slopes plunging 12° towards the east

and the west (Fig. S1b) and its surface presents corrugations extending perpendicular to the rift valley (Fig. S1a).

Sampling along the Doldrums transform recovered variably tectonized gabbros and peridotites from the northern and southern wall of the active transform valley (Pushcharovsky *et al.*, 1991, 1992; Skolotnev *et al.*, 2020). This study includes 9 gabbroic samples from the Doldrums transform walls (dredges S09-69, S09-76 and S09-81; Fig. 1b), namely 1 olivine gabbro, 5 gabbros, 2 gabbronorites and 1 oxide gabbro (Supplementary Table S1).

3.3. Vernadsky transform and Peyve Seamount

The Vernadsky transform offsets the ITR-1 and ITR-2 segments by 145 km. It is characterized by progressively shallower depths moving eastward from the nodal basin (6040 m; 38°W) along the active transform valley (Supplementary Figure S2a). The southern wall of the transform gently plunges into the valley (5-15°; Fig. S2b,c,d), whereas the northern wall of the transform is characterized by steep slopes (20-30°; Fig. S2b,c,d). The latter transform wall is also characterized by the occurrence of a large structural high named Peyve Seamount (from 37°50'W to 37°33'W) and of a well-developed volcanic fabric deepening into the transform valley (from 37°33'W to 37°20'W) (Fig. S2a).

Peyve Seamount, located 25 km to the east respect to the ITR-1 rift valley, is a 33 km-long and 8 km-wide prominent bathymetric high elongated along the Vernadsky transform wall. It is the shallowest portion of the entire Doldrums Megatransform System, rising 3700 m above the transform valley floor and reaching a minimum depth of 1033 m (Fig. 2a). It is characterized by a flat top, abruptly dipping between 21 and 34° into steep flanks on all sides (Fig. 2b,c,d). This bathymetric high deepens to the north into a well-developed volcanic fabric characterized by a succession of ridges and valleys parallel to the ITR-1 axis (Fig. 2a).

The sampling of the Vernadsky transform wall was deployed from the Vernadsky transform valley to the top of Peyve Seamount (Fig. 1b; Fig. 2d). Peridotites, variably evolved gabbros (Fig. 2e) and minor basalts were recovered (Pushcharovsky *et al.*, 1991, 1992; Skolotnev *et al.*, 2020). This study includes 45 samples from the northern wall of the Vernadsky transform (dredges S06-64, S09-61, S45-07, S45-08, S45-10; Fig. 1b), namely 6 olivine gabbros, 6 gabbros, 10 gabbronorites, 15 oxide gabbros and 8 basalts (Supplementary Table S1).

4. PETROGRAPHY

The studied gabbroic rocks range from olivine gabbros to gabbros *sensu stricto*, olivine gabbronorites, gabbronorites, oxide gabbronorites and oxide gabbros (Fig. 2e). Most of the studied gabbros have been sampled from the southern slope of the Peyve Seamount, where the high number and density of dredges deployed (Fig. 2d) along the transform valley likely allowed for a representative sampling of this portion of oceanic crust.

Olivine gabbros show a hypidiomorphic texture of millimetric olivine (5-10 vol%), plagioclase (50-55 vol%), clinopyroxene (35-40 vol%) and rare brown to dark green amphibole occurring at clinopyroxene rims (Fig. 3a,b). A single 500µm euhedral orthopyroxene crystal was found in an olivine gabbro sample (S45-7-2; Fig. 3a). Anhedral olivines commonly show irregular and lobate contacts with large plagioclase crystals (Fig. 3b). In places, plagioclase shows evidence of plastic deformation, with the occurrence of mechanical twins and undulose extinctions (Fig. 3b). Euhedral plagioclase laths are commonly found included in subhedral to anhedral clinopyroxene (Fig. 3b).

Gabbros sensu stricto show a hypidiomorphic texture of millimetric plagioclase (50-55 vol%) and clinopyroxene (45-50 vol%) (Fig. 3c). Some samples show the partial recrystallization of plagioclase into aggregates of 200-500 µm-size plagioclase neoblasts (Fig. 3c).

Gabbronorites, here referred to all samples containing more than 5 volume percent of orthopyroxene, range from olivine gabbronorites to gabbronorites and oxide gabbronorites. All samples are characterized by a hypidiomorphic texture of millimetric plagioclase (50-60 vol%), clinopyroxene (20-30 vol%) and orthopyroxene (5-14 vol%) (Fig. 4a), but olivine gabbronorites show the occurrence of olivine (5-8 vol%) and oxide gabbronorites the presence of Fe-Ti oxides (8-10 vol%) and brown amphibole (3-5 vol%) (Fig. 4b). Orthopyroxenes occur as millimetric to centimetric euhedral crystals in all gabbronoritic samples (Fig. 4a) and Fe-Ti oxides are interstitial in all oxide gabbronorites (Fig. 4b). Orthopyroxenes and clinopyroxenes are mostly undeformed (Fig. 4a), whereas plagioclase is partly recrystallized in places, forming aggregates of 200-500 µm-size plagioclase neoblasts (Fig. 4a,b). Notably, a sharp contact between gabbronorite and oxide gabbronorite has been sampled (S45-7-4B) and shows an irregular shape (Fig. S1a).

Oxide gabbros show a hypidiomorphic texture of millimetric plagioclase (50-60 vol%), clinopyroxene (25-30 vol%), Fe-Ti oxides (5-15 vol%) and minor orthopyroxene (0-5 vol%) and brown to dark green amphibole (3-5 vol%) (Fig. 4c,d). Fe-Ti oxides occur as interstitial crystals around euhedral plagioclase and subhedral clinopyroxene (Fig. 4c). Variations in grain size are observed at the scale of the thin section (S45-7-6A), between coarse-grained intervals presenting a

weak foliation of deformed plagioclase laths, and fine-grained granular domains (Fig. 4d). The fine-grained domains enclose partially corroded coarse-grained plagioclase laths similar to the crystals forming the coarse-grained oxide gabbro.

5. ANALYTICAL METHODS

5.1. Bulk-rock chemical compositions

Bulk-rock major element analyses were performed on 54 samples recovered in the ITR-1 domain during the S06, S09 and S45 campaigns (Supplementary Table S1), namely 45 samples from the Vernadsky transform wall, and 9 samples from the Doldrums transform walls (Fig. 1b). Internal portions of all gabbroic and basaltic rocks were crushed and pulverized in a tungsten carbide swing mill and analyzed at the Laboratory of chemical and analytical research of the Geological Institute, Russian Academy of Science (Moscow, Russia), using an S4 Pioneer X-Ray Fluorescence spectrometer (Bruker, Germany). Loss on Ignition (LOI) was defined by measuring the difference in mass of the powdered samples before and after being heated to 950°C for twelve hours in a chamber furnace. The Fe_2O_3 content of the whole-rock analyses has been converted to FeO using a conversion factor of 0.8998.

Bulk-rock trace element contents were determined on 26 samples recovered from the Vernadsky transform wall and 6 samples from the Doldrums transform walls (Supplementary Table S1). Powdered samples were dissolved using a mixture of hydrofluoric and nitric acids. The solution was subsequently evaporated with perchloric, boric and nitric acids and transferred into separate flasks using 3 % nitric acid and In as internal standard at the Laboratory of chemical and analytical research of the Geological Institute, Russian Academy of Science (Moscow, Russia). Sample analyses were carried out using an Element2 mass spectrometer (Thermo Fisher Scientific GmbH, Germany). Total analytical errors of the element analyses are within 10 %.

5.2. Mineral chemical compositions

Mineral major and trace element analyses were performed on 11 samples recovered from the southern slope of Peyve Seamount during Expedition S45, namely 2 olivine gabbros, 1 gabbro, 5 gabbronorites and 3 oxide gabbros.

Major element compositions (SiO_2, TiO_2, Al_2O_3, Cr_2O_3, FeO, MgO, MnO, CaO, NiO, Na_2O, K_2O, Cl) of plagioclase, clinopyroxene, orthopyroxene, olivine, amphibole and Fe-Ti oxides were analysed

by a JEOL JXA 8200 Superprobe equipped with five wavelength-dispersive (WDS) spectrometers, an energy dispersive (EDS) spectrometer, and a cathodoluminescence detector operating at the Dipartimento di Scienze della Terra, University of Milano, Italy. The analyses of all elements were performed with a 30-seconds counting time at an accelerating potential of 15 kV and a beam current of 15 nA.

Trace element compositions of clinopyroxene, plagioclase, orthopyroxene and amphibole were determined by Laser Ablation-Inductively Coupled Plasma-Mass Spectrometry (LA-ICP-MS) at CNR, Istituto di Geoscienze e Georisorse (Unità di Pavia). We used a PerkinElmer SCIEX ELAN DRC-e quadrupole mass spectrometer coupled with an UP213 deep-UV YAG Laser Ablation System (New Wave Research, Inc.). Laser (213nm wavelength) spot size was set to 100µm and the ablation frequency to 10 Hz, with a fluence of ~9.5 J/cm2. Helium was used as the carrier gas and was mixed with Ar downstream from the ablation cell. Data reduction was performed using the GLITTER software. NIST SRM 612 synthetic glass was used as the external standard, and CaO and SiO_2 concentrations previously measured by EPMA were used as the internal standard. The precision and accuracy of the trace element concentrations were assessed by repeated analyses of the BCR2-g standard and were better than ±7% and ±10%, respectively.

6. RESULTS

6.1. Bulk-rock major and trace element compositions

The studied gabbros define a wide range of bulk-rock compositions (Supplementary Table S1), from high Mg-values (Mg# = Mg/[Mg+Fe] mol%) in olivine gabbros (Mg# = 64.63-77.33), gabbros (Mg# = 57.92-77.69) and gabbronorites (Mg# = 56.37-79.81) to lower Mg-values in oxide gabbros (Mg# = 18.30-61.22) (Fig. 5a). Ca-values (Ca# = Ca/[Ca+Na] mol%) also show higher values for olivine gabbros (Ca# = 62.25-80.42) and slightly decrease from gabbros (Ca# = 56.14-75.09) to gabbronorites (Ca# = 53.10-73.22) and oxide gabbros (Ca# = 52.45-68.96) (Fig. 5a). The analysed samples define a compositional trend characterized by decreasing MgO and increasing FeO contents (Fig. 5b) from olivine gabbros (MgO = 9.27-13.96 wt%; FeO = 5.64-9.04 wt%) to gabbros (MgO = 7.02-10.14wt%; FeO = 3.70-10.02 wt%), gabbronorites (MgO = 6.40-11.00 wt%; FeO = 4.35-8.83 wt%), and oxide gabbros (MgO = 2.81-7.73 wt%; FeO = 8.73-22.67 wt%). Similarly, at decreasing MgO contents, the bulk-rock compositions of olivine gabbros, gabbros and gabbronorites show a progressive increase in SiO_2 (from 46.17 to 54.04 wt%; Fig. 6a), CaO (8.08-14.60 wt%; Fig. 6b), Al_2O_3 (10.99-19.03 wt%; Fig. 6c), TiO_2 (0.32-1.28 wt%; Fig. 6d), Na_2O (1.73-4.40 wt%; Fig. 6e). Oxide gabbros show a distinct compositional trend at decreasing MgO contents, in continuity with

the most evolved gabbros and gabbronorites; they show decreasing contents of SiO_2 (52.77-43.75 wt%; Fig. 6a), CaO (11.23-7.44 wt%; Fig. 6b), Al_2O_3 (15.79-10.19 wt%; Fig. 6c) and strong increase in TiO_2 (1.15-5.52 wt%; Fig. 6d) and Na_2O contents (2.45-4.00 wt%; Fig. 6e). All gabbroic samples show relatively homogeneous CaO/Al_2O_3 ratios (0.48-1.17; Fig. 6f).

The bulk-rock compositions of the studied samples fall in the composition field of the gabbros drilled at the Atlantis Massif in the Mid-Atlantic Ridge (Godard *et al.*, 2009) and at the Atlantis Bank in the Southwest Indian Ridge (Dick *et al.*, 2000) (Fig. 5, Fig. 6). Notably, the compositional field of the gabbros reported from the Atlantis Massif extends to more primitive compositions than the Atlantis Bank and the studied samples (i.e., higher Mg# and MgO contents; Fig. 5a,b). To compare the bulk composition of Vernadsky transform wall with that of the Atlantis Massif gabbros (Hole 1309D; Godard *et al.*, 2009) and the Atlantis Bank (Hole 735B; Dick *et al.*, 2000), we calculated the bulk composition of the Peyve Seamount, where 8 dredges were deployed along a single transect from the base of the transform wall to its top (Fig. 2d). The bulk composition was calculated based on the weighted average of all the gabbroic samples recovered, defining the bulk-rock chemical compositions of each lithology, that have been scaled to the mass fractions of the dredged samples (Fig. 2e; 28 wt% olivine gabbros, 13 wt% gabbros; 10 wt% gabbronorites, 49 wt% oxide gabbros; see Skolotnev *et al.*, 2020). According to this calculation, the bulk Peyve Seamount (orange star in Fig. 5) shows more evolved compositions than the calculated bulk composition of both Hole 1309D gabbros (light grey star in Fig. 5) and Hole 735B (dark grey star in Fig. 5), extending towards lower Mg- and Ca-values (Fig. 5a), lower MgO and higher FeO contents (Fig. 5b).

The studied gabbroic rocks also show large bulk-rock incompatible trace element compositional variability (Supplementary Table S1). REE concentrations increase from olivine gabbros (Yb_N = 7.86-8.14; $_N$ = normalized to C1-chondrite after Sun & McDonough, 1989) to gabbros (Yb_N = 5.53-10.55), gabbronorites (Yb_N = 6.37-37.40) and oxide gabbros (Yb_N = 7.13-29.70) (Fig. 7a,b). Olivine gabbros and gabbros show the lowest LREE/HREE fractionation (La_N/Yb_N = 0.33-0.68; Fig. 7a), whereas more variable LREE/HREE fractionation is observed in gabbronorites (La_N/Yb_N = 0.45-2.07; Fig. 7b) and oxide gabbros (La_N/Yb_N = 0.22-0.98; Fig. 7a). The most evolved gabbronorites are characterized by a negative Eu anomaly, whereas olivine gabbros, gabbros and oxide gabbros are characterized by positive Eu anomalies (Fig. 7a,b). Olivine gabbros, gabbros and gabbronorites show negative Ti, Zr and Hf anomalies, whereas oxide gabbros show positive anomalies for these elements (Fig. 7c,d).

The basalts recovered from Peyve Seamount (Supplementary Table S1) are characterized by variable major element bulk-rock compositions, from primitive to relatively evolved compositions (Mg# = 50.72-68.74; Ca# = 58.08-68.87). They show relatively flat REE patterns at low REE contents

316 (Yb_N = 13.98-33.82; La_N/Yb_N = 0.45-0.87) and no anomalies in highly incompatible elements respect
317 to N-MORB compositions (Workman and Hart, 2005).

318

319 **6.2. Mineral major and trace element compositions**

320 The mineral major element compositions of the gabbros from the Vernadsky transform wall are
321 consistent with those of the gabbros drilled at the Atlantis Massif along the Mid-Atlantic Ridge (Fig.
322 8; Miller *et al.*, 2009) and at the Atlantis Bank along the Southwest Indian Ridge (Fig. 8; Dick *et al.*,
323 2002).

324 *Clinopyroxenes* (Supplementary Table S2) show compositional trends defined by a positive
325 correlation between the Mg-value and the Al_2O_3 content (Fig. 8a), both higher in olivine gabbros
326 (Mg# = 74.60-80.30; Al_2O_3 = 2.33-3.15 wt%) and gabbros (Mg# = 78.69-81.32; Al_2O_3 = 2.27-2.74
327 wt%) respect to gabbronorites (Mg# = 58.89-78.07; Al_2O_3 = 1.01-2.80 wt%) and oxide gabbros (Mg#
328 = 57.08-78.07; Al_2O_3 = 0.97-2.50 wt%). TiO_2 contents initially increase at decreasing Mg-value,
329 before decreasing at lower Mg-values (Fig. 8b). Accordingly, clinopyroxenes analysed in olivine
330 gabbros (TiO_2 = 0.51-0.80 wt%) and gabbros (TiO_2 = 0.62-0.73 wt%) show higher TiO_2 contents
331 than the ones analysed in Fe-Ti oxide-bearing lithologies, i.e., the oxide gabbronorites (TiO_2 = 0.23-
332 0.92 wt%) and the oxide gabbros (TiO_2 = 0.24-0.90 wt%), as the result of Fe-Ti oxides co-saturation
333 (e.g., Dick *et al.*, 2002; Botcharnikov *et al.*, 2008).

334 Clinopyroxenes show strong trace element compositional variations mirroring the bulk-rock
335 compositional variability (Fig. 9a). Low REE concentrations and low LREE/MREE ratios
336 characterize the olivine gabbros (Yb_N = 10.89-19.32; La_N/Sm_N = 0.078-0.149) and gabbros (Yb_N =
337 10.71-15.57; La_N/Sm_N = 0.089-0.119), whereas high REE concentrations and relatively low
338 LREE/MREE ratios characterize the clinopyroxenes within oxide gabbros (Yb_N = 41.66-129.91;
339 La_N/Sm_N = 0.118-0.232). Clinopyroxenes in gabbronorites are distinct from those in the other
340 lithologies, with higher LREE/MREE ratios (Yb_N = 12.25-74.65; La_N/Sm_N = 0.109-0.490). All
341 clinopyroxenes from the analyzed gabbroic rocks show negative Eu and Sr anomalies, which become
342 increasingly marked at higher REE contents. Additionally, clinopyroxenes within gabbronorites also
343 display strong negative Ti anomalies (Fig. 9b) and some show negligible to slightly positive Zr-Hf
344 anomalies (Zr_N/Nd_N = 0.30-1.73), contrasting with the strongly negative Zr-Hf anomalies
345 characterizing all clinopyroxenes analysed within olivine gabbros, gabbros and oxide gabbros
346 (Zr_N/Nd_N = 0.29-0.85; Fig. 9b).

347 *Plagioclases* (Supplementary Table S3) show Anorthite contents (An = Ca/[Ca+Na] mol%) that
348 decrease at decreasing clinopyroxene Mg-values (Fig. 8c) and increasing K_2O contents (Fig. 8d),

from olivine gabbros (An = 52.80-70.01; K_2O = 0.03-0.07 wt%) to gabbros (An = 35.90-61.32; K_2O = 0.03-0.23 wt%), gabbronorites (An = 20.01-57.93; K_2O = 0.03-0.38 wt%) and oxide gabbros (An = 34.45-51.20; K_2O = 0.03-0.29 wt%).

Plagioclases within the olivine gabbros show low REE abundances (Ce_N = 1.37-1.90), whereas REE concentrations are higher and more variable in gabbros (Ce_N = 1.31-6.85), gabbronorites (Ce_N = 1.62-9.80) and oxide gabbros (Ce_N = 1.97-11.07) (Fig. 9c). All plagioclases show positive Eu, Sr and Ba anomalies (Fig. 9d).

Orthopyroxenes (Supplementary Table S4) show a positive correlation between Mg-values, Al_2O_3 (Fig. 8e) and TiO_2 contents (Fig. 8f), progressively decreasing from olivine gabbros (Mg# = 73.72; Al_2O_3 = 1.22 wt%; TiO_2 = 0.45 wt%) to gabbronorites (Mg# = 44.38-70.87; Al_2O_3 = 0.26-1.33 wt%; TiO_2 = 0.22-0.62 wt%) and oxide gabbros (Mg# = 47.58-59.60; Al_2O_3 = 0.45-1.34 wt%; TiO_2 = 0.20-0.54 wt%).

The orthopyroxene analysed within the olivine gabbro displays lower REE concentrations (Yb_N = 3.88) than the orthopyroxenes analysed within the gabbronorites (Yb_N = 5.17-12.62) and oxide gabbros (Yb_N = 8.25-15.39) (Fig. 9e). Although variable, some orthopyroxenes analysed in the gabbronorites show enrichments in Zr and Hf relative to neighbouring elements (Fig. 9f).

Amphiboles (Supplementary Table S5) are characterized by low silica contents and high TiO_2, alkaline (Na+K) and alumina contents (Si a.p.f.u. = 6.32-6.99; TiO_2 = 1.12-3.10 wt%; Na+K a.p.f.u. = 0.47-0.76; Al^{IV} a.p.f.u. = 1.01-1.679) and are classified as pargasite to edenite (classification after Leake *et al.*, 1997). Pargasites are mainly found as interstitial phases, although euhedral crystals locally occur within the oxide gabbros.

Pargasitic amphibole trace element compositions show increasing REE contents (Fig. 9g) from olivine gabbros (Yb_N = 11.51-22.34) to oxide gabbros (Yb_N = 34.21) and gabbronorites (Yb_N = 52.43-59.32). Notably, amphiboles within the gabbronorites show higher LREE/MREE ratios (La_N/Sm_N = 0.279-0.340) than amphiboles analysed in the olivine and oxide gabbros (La_N/Sm_N = 0.149-0.188) (Fig. 9g). Within the gabbronorites, amphiboles also show positive anomalies in Nb, Ta, Zr and Hf (Zr_N/Nd_N = 1.26-1.28; Fig. 9h), contrasting with the negative Zr-Hf anomalies characterizing amphiboles analysed within olivine gabbros and oxide gabbros (Zr_N/Nd_N = 0.40-0.64: Fig. 9h).

Olivines (Supplementary Table S6) show relatively low Mg-values and NiO contents in olivine gabbros (Mg# = 71.37-72.73; NiO = 0.02-0.13 wt%) and olivine-bearing gabbronorites (Mg# = 68.80-69.22; NiO = 0.01-0.10 wt%).

7. DISCUSSION

7.1. Composition of the oceanic crust exposed at oceanic transform walls

Extensive sampling of the Doldrums Megatransform System allowed to recover numerous gabbroic rocks from the ITR-1 domain, and more specifically from the edges of the ITR segment (Fig. 1b). The investigated gabbros were recovered in 3 dredges from the walls of the Doldrums transform valley (Fig. 1b) and 5 dredges from the Vernadsky transform valley that have been deployed on the southern slope of Seamount Peyve (Fig. 1b; Fig. 2d), sampling a complete transect of the Vernadsky transform wall (Fig. 1b).

The gabbros are characterized by a typical cumulate-like subophitic texture with the common occurrence of clinopyroxene oikocrysts including euhedral plagioclase chadacrysts (Fig. 3; Fig. 4), consistent with the expected low-pressure crystallization order of a MORB melt: olivine-plagioclase-clinopyroxene (e.g., Elthon *et al.*, 1992; Grove *et al.*, 1992). Their bulk-rock major element compositions define crystal lines of descent similar to those of the lower crustal sequence of IODP Site U1309 at the Atlantis Massif, located at 30°N along the Mid-Atlantic Ridge (Godard *et al.*, 2009) (Fig. 5; Fig. 6), although we emphasize important differences in the proportion of gabbroic lithologies.

IODP Site U1309 has been drilled in the central part of the Atlantis Massif OCC, 20 km from the transform valley. The drillhole consists in a large variety of gabbros ranging from olivine-rich troctolites to oxide gabbros, and the bulk Hole composition compares to that of a primitive N-MORB melt (Godard *et al.*, 2009). Conversely, the gabbros collected along the walls of the Doldrums and Vernadsky transforms lack the most primitive gabbroic endmembers such as dunites and troctolites (Fig. 5) but are instead characterized by a large proportion of chemically evolved oxide-bearing gabbros and gabbronorites (49 wt% at Peyve Seamount; Fig. 2e; Fig. 5; Fig. 6). Yet, based on *MELTS* calculations, Sanfilippo *et al.* (2019) quantified that oxide gabbros are expected to represent less than ~20 wt% of the gabbros fractionated by a primitive MORB melt. The calculated Peyve Seamount bulk composition (Mg# = 57; Ca# = 66) is also markedly more evolved than that of Atlantis Massif Hole 1309D (Mg# = 73; Ca# = 77), although they follow similar crystal lines of descent (Fig. 5). The excess in Fe-Ti oxides of the gabbros sampled along the Vernadsky and Doldrums transform walls points to an overall evolved composition of the gabbroic layer, that may in turn suggest some extent of fractionation of the parental melts prior to their emplacement within the transform domain.

In the vicinity of a ridge-transform intersection, seafloor spreading is mainly accommodated by tectonic extension; the lithosphere is thicker and melt production is scarce (e.g., Hooft *et al.*, 2000; Behn and Ito, 2008; Bai and Montési, 2015). Additionally, the cold edge effect induced by large-offset transform faults can lead to further thickening of the oceanic lithosphere and a progressive

decrease in melt productivity along the ridge axis (Ligi *et al.*, 2002, 2005). In such a cold oceanic environment characterized by a thick lithosphere, melt production may cease at high pressure (□8-10 kbar; e.g., Langmuir and Forsyth, 2007) and melts need to migrate for greater distances before pooling in shallow magma chambers to form the gabbroic crust (e.g., Niu, 2021). Therefore, one possibility to explain the distinctly evolved composition of the gabbroic crust in this region is that primary melts could have undergone chemical evolution during their migration through a thick lithosphere, at depths greater than the exposed gabbroic crust (< 2 kbar; "*High-pressure differentiation*" in Fig. 10; e.g., Warren and Shimizu, 2010; Bennett *et al.*, 2019). Yet, the basalts recovered on top of Peyve Seamount show primitive compositions (Mg# > 67; Supplementary Table S1) indicating that melts produced beneath the transform wall experienced limited differentiation during their migration from the source region. Additionally, high melt supply along the entire ITR-1 is evidenced by a well-developed volcanic fabric immediately north of Peyve Seamount and south of the Doldrums transform wall (Fig. 1b; Fig. 3a). We therefore infer that the juxtaposition of the ridge axis with the □12 and □10 Ma lithosphere across the Doldrums and Vernadsky transforms, respectively, did not strongly reduce melt production in the underlying mantle. We thus exclude that primary melts might have extensively fractionated during migration through a thick lithosphere before forming the gabbroic crust in this transform domain.

Alternatively, the abundance of Fe-Ti oxides in the gabbroic crust sampled at the transform walls can be explained by processes of lateral differentiation (e.g., Dick *et al.*, 2019; Brunelli *et al.*, 2020). This process implies that melts produced in the most peripheral parts of the melting region beneath a ridge segment can be focused towards the actively deforming lithosphere in the vicinity of the ridge-transform intersection and be emplaced along the transform domain ("*Lateral differentiation*" in Fig. 10; see Brunelli *et al.*, 2020). These melts experience extensive fractionation prior to their intrusion into the transform wall, producing a lower oceanic crust distinctly enriched in Ti-Fe oxides. In the following, we will show that such a process of lateral melt migration, locally associated to melt-rock reactions, accounts for the compositions of the gabbroic crust sampled at the Doldrums and Vernadsky transform walls.

7.2. Lateral melt differentiation as a ubiquitous process at slow-spreading transform faults

Evolved compositions of the gabbroic crust sampled along transform walls have been previously documented in other slow- to ultraslow-spreading environments worldwide, such as the Atlantis Bank (e.g., Dick *et al.*, 2019) and the Vema Lithospheric Section (Brunelli *et al.*, 2020). At the Atlantis Bank along the Southwest Indian Ridge, extensive dredging, diving, and drilling evidenced a compositional zonation both laterally and vertically, with a vast majority of olivine gabbros

450 characterizing the centre of the gabbroic body (i.e., ODP Hole 735B and IODP Hole U1473A) and a
451 high proportion of oxide gabbros towards the exterior (e.g., Dick *et al.*, 2000, 2002, 2019; MacLeod
452 *et al.*, 2017). This lithological zonation is believed to result from progressive differentiation of the
453 melts away from the core of the Atlantis Bank gabbroic massif, where melts are transported from the
454 mantle to the crust (see Dick *et al.*, 2019). Thus, the evolved composition of the gabbroic crust
455 sampled along the Atlantis II transform wall results from processes of lateral melt migration and
456 differentiation. Along the Vema Fracture Zone, extensive sampling allowed to document a complete
457 section of oceanic lithosphere, from residual peridotites to intrusive gabbros and extrusive volcanics
458 (Auzende *et al.*, 1989; Cannat *et al.*, 1991; Brunelli *et al.*, 2020). The gabbros exposed there are
459 strongly evolved, showing widespread occurrence of Fe-Ti oxides and apatite. Brunelli *et al.* (2020)
460 interpreted the excess in oxide gabbros as the result of lateral differentiation of melts migrating from
461 the magmatically robust segment centre to the magma-poor ridge-transform intersection. Therefore,
462 the evolved composition of the gabbroic crust sampled along the Atlantis II and Vema transform
463 appears to be a direct consequence of lateral differentiation processes and the scarce magmatism in
464 the vicinity of the transform zone, similar to what we document at the ITR-1 (Fig. 10). We emphasize,
465 however, that such processes of lateral melt migration most likely occur only at segment edges; the
466 well-documented Atlantis Bank (e.g., Dick *et al.*, 2019) allows to constrain the extent of such
467 processes to few tens of kilometers from the transform at most. This in turn implies that the melts
468 migrating laterally do not necessarily originate at the centre of a ridge segment, as it was inferred by
469 Brunelli *et al.* (2020), but simply from magmatically productive peripheral portions of the melting
470 region, close to the transform zone (Fig. 10).
471 Additionally, numerous accounts of evolved oxide-rich gabbroic crust sampled along transform
472 walls have been documented in slow-spreading environments worldwide, although not investigated
473 in detail, namely along: *i)* Andrew Bain (Southwest Indian Ridge; Takeuchi *et al.*, 2010); *ii)* Mado
474 Megamullion (Philippine Sea; Basch *et al.*, 2020; Akizawa *et al.*, 2021); *iii)* Atlantis (Atlantis Massif,
475 Mid-Atlantic Ridge, e.g., Blackman *et al.*, 2002, 2011; Boschi *et al.*, 2006; Karson *et al.*, 2006), and
476 i*v)* Kane (Mid-Atlantic Ridge, e.g., Mével *et al.*, 1991; Auzende *et al.*, 1994; Dick *et al.*, 2008).
477 Lateral melt migration and formation of gabbroic crust with anomalously evolved composition
478 therefore appears to be a common, if not ubiquitous characteristic of the lower oceanic crust sampled
479 along transform walls at slow-spreading ridges (Fig. 10).
480

481 **7.3. Reactive melt migration and formation of gabbronorites: the case of the Peyve Seamount**

482 The gabbroic rocks sampled on the southern slope of Peyve Seamount range from olivine gabbros
483 (Fig. 3a,b) to gabbros *sensu stricto* (Fig. 3c), gabbronorites (Fig. 4a,b) and oxide gabbros (Fig. 4c,d).

They are characterized by the widespread occurrence of centimetric euhedral orthopyroxenes (Fig. 4) in numerous olivine gabbronorites, gabbronorites and oxide gabbronorites, which is not common in oceanic settings (e.g., Grove *et al.*, 1992). In MORB-type environments, orthopyroxene is mostly documented as a late-stage magmatic phase, crystallizing interstitial and vermicular crystals around the primary magmatic phases during the closure of the magmatic system at near-solidus temperatures (e.g., Natland *et al.*, 1991; Ozawa *et al.*, 1991; Feig *et al.*, 2006; Botcharnikov *et al.*, 2008; Koepke *et al.*, 2018; Zhang *et al.*, 2020). To date, orthopyroxenes occurring as a primary magmatic phase have been reported in gabbroic rocks as a result of: *i)* interaction between percolating melts and host peridotites, leading to partial dissolution of the peridotite and to the saturation of orthopyroxene in the reactive melt (e.g., Dick and Natland, 1996; Coogan *et al.*, 2002; Suhr *et al.*, 2008; Sanfilippo *et al.*, 2016); *ii)* crystallization of depleted melts formed during shallow peridotite melting (e.g., Gillis *et al.*, 2014); *iii)* interaction between an olivine-rich gabbroic matrix and an evolved percolating melt (Bloomer *et al.*, 1991; Zellmer *et al.*, 2016; Gardner *et al.*, 2020; Zhang *et al.*, 2020).

The bulk-rock compositions of the gabbroic lithologies recovered along the Doldrums and the Vernadsky transforms define compositional trends that suggest progressive evolution of the parental melt composition from olivine gabbro to gabbro, gabbronorite and oxide gabbro (Fig. 5; Fig. 6; Fig. 7). In order to assess the evolution of the parental melt composition and constrain the process responsible for the saturation of primary orthopyroxene, we computed the trace element composition of the parental melts from the different lithologies recovered. The composition of melts calculated in equilibrium with clinopyroxene crystal cores (Supplementary Table S7), using the compilation of partition coefficients from Basch *et al.* (2018), are shown in Figure 11. The melts in equilibrium with the olivine gabbros and gabbros are characterized by MORB-type compositions (Ce_N/Yb_N = 0.764-1.476; La_N/Sm_N = 0.433-0.826; Fig. 11a), with LREE/MREE fractionation similar to a typical N-MORB (after Workman and Hart, 2005) and to the basalts recovered from the top of Peyve Seamount (Fig. 11a). However, upon differentiation of the parental melt, the progressive enrichment in REE concentrations appears to have been accompanied by Zr-Hf enrichments and variations in the LREE/MREE and LREE/HREE ratios. The parental melts of oxide gabbros show weak Zr-Hf and LREE enrichments (Ce_N/Yb_N = 1.302-2.050; La_N/Sm_N = 0.657-1.291; Zr_N/Nd_N = 0.434-1.273; Fig. 11a), whereas the parental melts of the gabbronorites are characterized by strong Zr-Hf and LREE enrichments (Ce_N/Yb_N = 0.959-4.776; La_N/Sm_N = 0.606-2.721; Zr_N/Nd_N = 0.457-2.602; Fig. 11b). Since the strongest preferential enrichments in highly incompatible trace elements are found in the orthopyroxene-bearing samples, we infer that the same petrological process responsible for the saturation in primary orthopyroxene triggered the enrichments in highly incompatible trace elements.

Several processes have been proposed to explain highly incompatible trace element enrichments in mineral phases, with different implications for the evolution of the magmatic system: *i)* diffusive reequilibration at sub-solidus conditions (e.g., Coogan and O'Hara, 2015); *ii)* trapped melt crystallization (e.g., Bédard, 1994; Elthon *et al.*, 1992), and *iii)* reactive melt migration (e.g., Coogan *et al.*, 2000; Sanfilippo *et al.*, 2020; Ferrando *et al.*, 2021a). Nonetheless, textural and geochemical arguments rule out the processes of diffusive reequilibration and melt entrapment as responsible for the presence of orthopyroxene and trace element enrichments. Namely, diffusion leads to the progressive reequilibration of mineral compositions at subsolidus temperature conditions (e.g., Costa *et al.*, 2020). This process could account for mineral trace element enrichments and variations in REE fractionation. However, subsolidus reequilibration processes would not lead to any modification in the modal composition and bulk-rock major and trace element compositions. Rather, the documented bulk-rock enrichments in highly incompatible elements (Fig. 7) require an open-system process and the input of a metasomatic component (e.g., Sanfilippo *et al.*, 2020). Accordingly, *in situ* crystallization of trapped melt could lead to strong mineral and bulk-rock enrichments in highly incompatible elements within a crystallizing gabbroic mush (e.g., Bédard, 1994). Closed-system melt differentiation could lead to orthopyroxene saturation and reproduce the LREE and HFSE enrichments reported in the studied samples. However, the occurrence of euhedral centimetre-size orthopyroxene in gabbronorites (Fig. 4a,b) and the strong trace element enrichments observed within both rims and cores of clinopyroxene crystals (Fig. 9a,b; Fig. 11b) are not consistent with the interstitial character of trapped melt crystallization. We thereby infer that the early saturation of orthopyroxene and the enrichments in highly incompatible trace elements most likely result from a modification of the parental melt composition driven by reactive migration of the parental melts.

Melts computed in equilibrium with the olivine gabbros and gabbros are characterized by MORB-type compositions (Fig. 11a), whereas the melts in equilibrium with the gabbronorites and oxide gabbros show variable enrichments in highly incompatible trace elements (Fig. 11a,b). This suggests that the inferred reactive migration process progressively modified the melt composition upon differentiation and reaction. Although interaction between mantle peridotites and MORB-type melts has been widely documented as a process driving orthopyroxene saturation in the reacted melt (e.g., Dick and Natland, 1996; Coogan *et al.*, 2002; Suhr *et al.*, 2008; Sanfilippo *et al.*, 2016; Zhang *et al.*, 2020), partial dissolution of the LREE-depleted phases forming the mantle peridotites, namely olivine, orthopyroxene and minor clinopyroxene, would further deplete the melt in the most incompatible trace elements. This is in contradiction with the enrichments in highly incompatible elements documented in the studied gabbronorites and oxide gabbros (Fig. 11), in turn suggesting that the documented reactive melt migration process did not involve partial dissolution of mantle

peridotites. Alternatively, dissolution of plagioclase and olivine from partly crystallized gabbroic crystal mushes have been widely documented in abyssal gabbros where, when coupled to the crystallization of new phases, it causes preferential enrichments in the most incompatible trace elements in the reacted melt (e.g., Lissenberg and MacLeod, 2016; Lissenberg *et al.*, 2019; Sanfilippo et al., 2020). Melt-mush reactions have been ubiquitously documented in the gabbros from the Mid-Atlantic Ridge (Coogan *et al.*, 2000; Lissenberg and Dick, 2008; Brunelli *et al.*, 2020), the Southwest Indian Ridge (Boulanger *et al.*, 2020; Sanfilippo *et al.*, 2020; Zhang *et al.*, 2020, 2021, Ferrando *et al.*, 2021a, 2021b), the East Pacific Rise (Hess Deep: Lissenberg *et al.*, 2013), and several ophiolitic occurrences (e.g., Bédard and Hébert, 1996; Liu et al., 2018; Tribuzio *et al.*, 2020; Basch *et al.*, 2022). Moreover, at the Atlantis Bank OCC, Gardner *et al.* (2020) and Zhang *et al.* (2020) documented the occurrence of substantial amounts of orthopyroxene in deformed olivine gabbros. They interpreted these distinct modal compositions as resulting from reactions between an oxide-saturated melt and a primitive gabbroic crystal mush. Yet, the possibility that orthopyroxene saturation resulted from melt-rock reaction has not been explored in detail and is merely inferred.

7.3.1. Modeling reaction-driven orthopyroxene saturation

In order to assess whether partial dissolution of a primitive gabbroic crystal mush is able to drive orthopyroxene saturation during fractionation of evolved MORB-type melts, we performed thermodynamic modeling of reactive fractional crystallization using the *MELTS* software (Ghiorso and Sack, 1995). The composition of the basalt S45-07-173, a relatively evolved N-MORB (Mg# = 56.78; Ca# = 66.15) sampled at the Seamount Peyve (Fig. 1b), has been selected as the starting melt composition. We computed a fractional crystallization process at a constant pressure of 2 kbar and temperatures decreasing from 1160°C to 1050°C with cooling steps of 5°C. Different models have been performed, involving the assimilation of various quantities of a primitive gabbroic crystal mush (ol:plg:cpx = 10:50:40 vol%), from 0.5g/°C of cooling to 2g/°C (Supplementary Table S8). Figure 12 compares the evolution of the modal composition of the solids fractionated in all models. Simple fractional crystallization leads to the formation of an oxide gabbro (plg:cpx:ox = 45:43:12 vol% at 1050°C; Fig. 12a), whereas the models involving assimilation of a primitive gabbroic mush show the early saturation of orthopyroxene upon fractionation. Notably, orthopyroxene appears as a liquidus phase at higher temperatures for higher assimilated masses (Fig. 12b-e). At assimilation rates of 0.5g/°C, orthopyroxene fractionates from 1085°C and the reactive crystallization process leads to the formation of an orthopyroxene-bearing oxide gabbro (pl:cpx:opx:ox = 45:47:4:4 vol% at 1050°C; Fig. 12b). At higher assimilation rates (2g/°C), orthopyroxene saturates at 1145°C and the reactive crystallization process leads to the formation of a gabbronorite (pl:cpx:opx:ox = 43:40:14:3 vol% at

1050°C; Fig. 12e). Interestingly, the saturation temperature of orthopyroxene in all models corresponds to the temperature at which the ratio between the assimilated mass and the crystallized mass reaches Ma/Mc = 0.7. The higher is this ratio, the stronger will be the influence of the assimilation process on the melt evolution. The results of these thermodynamic models therefore suggest that, at high assimilation rates, the partial dissolution of a primitive gabbroic crystal mush during concomitant fractionation of an evolved MORB-type melt allows for the early saturation of orthopyroxene in the reacted melt.

7.3.2. Modeling of reaction-driven trace element enrichments

We infer that a process of reactive melt migration, during which an evolved melt partially assimilates a primitive crystal mush, is responsible for both the saturation of primary orthopyroxene and the strong highly incompatible trace element (LREE, HFSE) enrichments documented in the gabbronorites (Fig. 7b; Fig. 11b). Accordingly, we selected similar parameters to the previous *MELTS* thermodynamic models to perform trace element modeling of Assimilation-Fractional Crystallization (AFC). Given that our aim is to reproduce mathematically the enrichments in highly incompatible elements driven by the well-constrained petrological process leading to orthopyroxene saturation, we chose to model AFC processes using the equation of De Paolo (1981), instead of more complex geochemical and thermodynamic models available in literature (e.g., Magma Chamber Simulator, see Bohrson *et al.*, 2014, 2020; Heinonen *et al.*, 2020).

The trace element composition of the basalt S45-07-173 (Yb_N = 24.8; La_N/Yb_N = 0.71) was chosen as starting melt composition, and the assimilated rock is a primitive gabbroic crystal mush, similar to the previous *MELTS* models (ol:plg:cpx = 10:50:40 vol%). We computed fractional crystallization assuming concomitant assimilation at Ma/Mc ratios ranging from 0 to 0.9. Since the AFC models do not provide thermodynamic constraints on the fractionated phases, we used the previous MELTS models to define the modal composition of the fractionated phases at a given Ma/Mc ratio. Namely, we modeled the fractionation of an oxide gabbro (plg:cpx:ox = 50:45:5 vol%) at Ma/Mc < 0.7 and the fractionation of a gabbronorite (plg:cpx:opx:ox = 50:40:8:2 vol%) at Ma/Mc > 0.7.

Figure 13 compares the composition of clinopyroxenes analyzed within the studied samples with the compositional trends of clinopyroxenes computed in equilibrium with the fractionating melt, at variable Ma/Mc ratios. The computed compositional trends clearly indicate that LREE/MREE ratios do not substantially vary during a fractional crystallization process (FC in Fig. 13), whereas strong enrichments in LREE respect to M-HREE are produced at high Ma/Mc ratios (Fig. 13). Notably, the threshold of Ma/Mc ratio observed for orthopyroxene saturation in the MELTS models is consistent with the computed trends of clinopyroxene compositions, i.e., clinopyroxenes analyzed within the

gabbronorites show high LREE/MREE ratios and plot above the threshold trend of Ma/Mc = 0.7, whereas clinopyroxenes analyzed within the oxide gabbros are characterized by low values of LREE/HREE fractionation, high HREE contents and plot below the threshold of Ma/Mc = 0.7 (Fig. 13).

To better visualize the evolution of the trace element compositions within the reacted melt upon differentiation (i.e., at decreasing melt mass and temperature), we plotted the detailed trace element evolution along two AFC trends representative of the formation of oxide gabbros (plg:cpx:ox = 50:45:5 vol%) and gabbronorites (plg:cpx:opx:ox = 50:40:8:2 vol%) (Supplementary Table S8). Consistently with the compositional trends documented in Figure 13, reactive crystallization of oxide gabbros and gabbronorites, involving low (Ma/Mc = 0.3; Fig. 14a) and high (Ma/Mc = 0.8; Fig. 14b) assimilated mass, respectively, reproduce well the trace element patterns of the melts computed in equilibrium with clinopyroxene cores (Fig. 14). Notably, the high LREE/MREE fractionation documented in the gabbronorites is caused by a lower increase in MREE-HREE upon progressive differentiation (Fig. 14b). Our thermodynamic and geochemical models therefore indicate that a process of assimilation of primitive gabbroic crystal mush within an evolved MORB-type melt can be responsible for the early saturation of orthopyroxene (Fig. 12), the increase in LREE/M-HREE ratios and the high HFSE contents (Fig. 13; Fig. 14b).

7.4. Melt-rock reaction as a ubiquitous process forming oceanic gabbronorites?

This study documents a well-constrained reaction-driven formation process for oceanic gabbronorites and related oxide gabbro(norite)s, the assimilated mass and the Ma/Mc ratio being the driving parameters of orthopyroxene saturation. In the context of transform walls, the process of melt/rock reaction accompanied lateral differentiation of the melts produced at the edges of the ridge segment (Fig. 10; e.g., Brunelli *et al.*, 2020). Notably, melt migration and concomitant lateral differentiation increase the chemical gradient between the percolating melt and the host rock, and therefore facilitates dissolution-precipitation reactions between a hot and primitive gabbroic crystal mush and invading melts (Fig. 15a; e.g., Liang, 2003). Diffuse percolation of the reactive melts in a hot system (Fig. 15a) is further supported by an irregular contact found between gabbronoritic and oxide gabbro portions of a studied thin section (S45-7-4B; Fig. S3a). Across this lithological contact, drastic within-sample variations in clinopyroxene core REE compositions (La_N/Sm_N = 0.118-0.490; Fig. S3b,c) point to millimetre-scale variations in assimilated mass, with Ma/Mc varying from 0 to 0.9 (Fig. S3c); the assimilated mass controls the formation of either a gabbronoritic assemblage or an oxide gabbro. This local melt hybridization implies that the chemical evolution of the melt was isolated at the scale of

millimetric apophyses (Fig. 15b), each characterized by its intrinsic reactivity towards the primitive gabbroic mush, as a function of the melt composition and temperature (e.g., Liang, 2003).

It is worth noting that although melt hybridization is facilitated by the high reactivity of the melts migrating laterally at segment edges, the reactive formation of gabbronorites is not limited to transform walls. Gabbronoritic samples from IODP Hole U1473A (Atlantis Bank, Southwest Indian ridge) were interpreted as formed after reaction between a gabbroic crystal mush and an evolved percolating melt (i.e., Zhang *et al.*, 2020). These gabbronorites show La_N/Sm_N ratios in clinopyroxene similar to the compositions analysed in the gabbronorites from Peyve Seamount (Fig. 13). This indicates an elevated assimilated mass and Ma/Mc ratios (Ma/Mc = 0.8-0.9) during reactive crystallization of the gabbronorites from the Atlantis Bank, in turn suggesting that the reactive processes documented in this study occur in the core of the Atlantis Bank gabbroic section as well. At IODP Hole 1309D (Atlantis Massif, Mid-Atlantic ridge), gabbronorites have been documented in the lower part of the drillcore (depth > 620 mbsf; Suhr *et al.*, 2008; Godard *et al.*, 2009). These gabbronorites show bulk-rock major and trace element compositions as primitive as the olivine gabbros and gabbros from Hole 1309D and are often associated with olivine-rich troctolites. The latter lithology has been extensively studied in recent years and has been interpreted as the replacive product of melt-rock interaction between a percolating melt and the host mantle peridotite (e.g., Suhr *et al.*, 2008; Drouin *et al.*, 2009; Ferrando *et al.*, 2018, 2020). We here infer that the common association between gabbronorites and olivine-rich troctolites is not fortuitous. The reactive formation of olivine-rich troctolites and the related dissolution of mantle orthopyroxene drove orthopyroxene saturation within the residual melt, that subsequently led to the formation of gabbronorites instead of gabbros (Collier and Kelemen, 2010; Sanfilippo *et al.*, 2016). The formation of gabbronorites from the Atlantis Massif thus did not involve reaction with a gabbroic crystal mush, but we emphasize that it resulted from the reaction between a percolating melt and its host peridotite, thus corroborating a ubiquitous reactive origin of gabbronorites from MORB melts in oceanic environments. Conversely, at the Vema Lithospheric Section (Mid-Atlantic ridge), most gabbros show an elevated modal content in Fe-Ti oxides, and only few samples show the occurrence of orthopyroxene. Although Brunelli *et al.* (2020) interpreted the origin of these oxide gabbros to be related with melt-mush interactions, they did not report the incompatible trace element compositions of the rock-forming minerals, precluding a direct comparison with our results. Yet, considering the output of our models (Fig. 12; Fig. 13, Fig. 14), we can infer that the reactive processes forming the oxide gabbros at the Vema transverse ridge did not involve extensive assimilation (Ma/Mc < 0.7) and therefore did not allow for the saturation of orthopyroxene in the reacted melt. Therefore, we here propose that the genesis of oceanic gabbronorites by melt-rock reaction can be a ubiquitous process

686 in the oceanic lithosphere but requires substantial amounts of assimilation to allow for early
687 orthopyroxene saturation.
688

689 **8. CONCLUSIONS**

690 The gabbroic crust recovered along the Doldrums and Vernadsky transforms shows an evolved
691 bulk composition, suggesting some extent of fractionation of the parental melts prior to their intrusion
692 and exhumation at transform valley walls. The excess in Fe-Ti oxides in the gabbroic rocks can be
693 explained by lateral differentiation of MORB melts during their migration from the segment edges
694 towards a ridge-transform intersection, as previously reported in other gabbroic occurrences from
695 transform valley walls worldwide. Additionally, the studied gabbroic sequence shows common
696 occurrence of coarse-grained euhedral orthopyroxene, which presence is not predicted during
697 fractional crystallization of tholeiitic melts. The gabbronorites also show preferential enrichments in
698 highly incompatible trace elements (LREE, HFSE) relative to the neighbouring trace elements,
699 evidenced in both bulk-rock and mineral compositions. Thermodynamic *MELTS* models and AFC
700 calculations coherently show that reaction of an evolved MORB melt, invading and partially
701 assimilating a primitive gabbroic crystal mush, can trigger the early saturation of primary
702 orthopyroxene and lead to preferential enrichments in LREE and HFSE in the crystallizing phases.
703 This study therefore documents a well-constrained case in which oceanic gabbronorites are produced
704 by melt-rock interaction processes, the assimilated mass being the driving parameter for
705 orthopyroxene saturation. Reactive melt migration is likely a consequence of lateral differentiation
706 processes, themselves enhanced by the low melt production beneath ridge-segment edges and by the
707 active tectonics in the transform domain. However, we infer that the genesis of gabbronorites by melt-
708 rock reaction is not limited to oceanic transforms but is likely ubiquitous in the oceanic lithosphere.
709

710 **ACKNOWLEDGEMENTS**

711 We would like to thank the captain, the officers, and the crew of *R/V Akademik Nikolaj Strakhov*. We
712 also thank Andrea Risplendente for his assistance with EPMA analyses at Università degli Studi di
713 Milano, as well as Antonio Langone for his assistance with the LA-ICP-MS analyses at the CNR-
714 IGG, Unità di Pavia.
715

FUNDING

This research was supported by the Italian Programma di Rilevante Interesse Nazionale through the grant [PRIN 2017 Prot.2017KX5ZX8], by the Accordo Bilaterale CNR/RFBR 2018-2020 through the grant [CUPB36C17000250005], by the Russian Foundation for the Basic Research project no. [18-55-7806 Ital_t], and by the Russian Basic Research Program projects no. [0135-2019-0050, FMMG-2022-0003].

REFERENCES

Akizawa, N., Ohara, Y., Okino, K., Ishizuka, O., Yamashita, H., Machida, S., Sanfilippo, A., Basch, V., Snow, J. E., Sen, A., Hirauchi, K., Michibayashi, K., Harigane, Y., Fujii, M., Asanuma, H. & Hirata, T. (2021). Geochemical characteristics of back-arc basin lower crust and upper mantle at final spreading stage of Shikoku Basin: an example of Mado Megamullion. *Progress in Earth and Planetary Science*, **8**, 65, doi: 10.1186/s40645-021-00454-3.

Auzende, J.-M., Bideau, D., Bonatti, E., Cannat, M., Honnorez, J., Lagabrielle, Y., Malavieille, J., Mamaloukas-Frangoulis, V. & Mevel, C. (1989). Direct observation of a section through slow-spreading oceanic crust. *Nature*, **337**, 726-729, doi: 10.1038/337726a0.

Auzende, J. M., Cannat, M., Gente, P., Henriet, J. P., Juteau, T., Karson, J., Lagabrielle, Y., Mével, C. & Tivey, M. (1994) Observation of sections of oceanic crust and mantle cropping out on the southern wall of Kane FZ (N. Atlantic). *Terra Nova*, **6**, 143-148.

Bai, H. & Montési, L. G. J. (2015). Slip-rate-dependent melt extraction at oceanic transform faults. *Geochemistry, Geophysics, Geosystems*, **16**, 401-419, doi: 10.1002/2014GC005579.

Basch, V., Rampone, E., Crispini, L., Ferrando, C., Ildefonse, B. & Godard, M. (2018). From mantle peridotites to hybrid troctolites: textural and chemical evolution during melt–rock interaction history (Mt. Maggiore, Corsica, France). *Lithos*, **323**, 4–23, doi: 10.1016/j.lithos.2018.02.025.

Basch, V., Rampone, E., Borghini, G., Ferrando, C. & Zanetti, A. (2019a). Origin of pyroxenites in the oceanic mantle and their implications on the reactive percolation of depleted melts. *Contributions to Mineralogy and Petrology*, **174**, 97, doi: 10.1007/s00410-019-1640-0.

Basch, V., Rampone, E., Crispini, L., Ferrando, C., Ildefonse, B. & Godard, M. (2019b). Multi-stage reactive formation of troctolites in slow-spreading oceanic lithosphere (Erro-Tobbio, Italy): a combined field and petrogeochemical study. *Journal of Petrology*, **60**, 873-906, doi: 10.1093/petrology/egz019.

Basch, V., Sanfilippo, A., Sani, C., Ohara, Y., Snow, J., Ishizuka, O., Harigane, Y., Michibayashi, K., Sen, A., Akizawa, N., Okino, K., Fujii, M. & Yamashita, H. (2020). Crustal accretion in a slow-spreading back-arc basin: Insights from the Mado Megamullion oceanic core complex in the Shikoku Basin. *Geochemistry, Geophysics, Geosystems*, **21**, e2020GC009199, doi: 10.1029/2020gc009199.

Basch, V., Sanfilippo, A., Vigliotti, L., Langone, A., Rasul, N., Khorsheed, M., AlNomani, S., AlQutub, A. & Ligi, M. (2022). Crustal contamination and hybridization of an embryonic oceanic crust during the Red Sea rifting (Tihama Asir igneous complex, Saudi Arabia). *Journal of Petrology*, in press, doi: 10.1093/petrology/egac005

Bédard, J. H. (1994). A procedure for calculating the equilibrium distribution of trace elements among the minerals of cumulate rocks, and the concentration of trace elements in coexisting liquids. *Chemical Geology*, **118**, 143-153, doi: 10.1016/0009-2541(94)90173-2.

Bédard, J. H., & Hébert, R. (1996). The lower crust of the Bay of Islands ophiolite, Canada: Petrology, mineralogy and the importance of syntexis in magmatic differentiation. *Journal of Geophysical Research*, **101**, 25105-25124.

Behn, M. D. & Ito, G. (2008). Magmatic and tectonic extension at mid-ocean ridges: 1. Controls on fault characteristics. *Geochemistry, Geophysics, Geosystems*, **9**, Q08O10, doi: 10.1029/2008GC001965.

Bennett, E. N., Jenner, F. E., Millet, M.-A., Cashman, K. V. & Lissenberg, C. J. (2019). Deep roots for mid-ocean-ridge volcanoes revealed by plagioclase-hosted melt inclusions. *Nature*, **572**, 235-239, doi: 10.1038/s41586-019-1448-0

Bickert, M., Cannat, M., Tommasi, A., Jammes, S. & Lavier, L. (2021). Strain localization in the root of detachment faults at a melt-starved mid-ocean ridge: a microstructural study of abyssal peridotites from the Southwest Indian Ridge. *Geochemistry, Geophysics, Geosystems*, **22**, e2020GC009434., doi: 10.1029/2020GC009434.

Blackman, D. K., Karson, J. A., Kelley, D. S., Cann, J. R., Früh-Green, G. L., Gee, J., S., Hurst, S. D., John, B. E., Morgan, J., Nooner, S. L., Ross, D. K., Shroeder, T. J. & Williams, E. A. (2002). Geology of the Atlantis Massif (Mid-Atlantic Ridge, 30° N): Implications for the evolution of an ultramafic oceanic core complex. *Marine Geophysical Researches*, **23**, 443-469, doi: 10.1023/B:MARI.0000018232.14085.75.

Blackman, D. K., Ildefonse, B., John, B. E., Ohara, Y., Miller, D. J., Abe, N., Abratis, M., Andal, E. S., Andreani, M., Awaji, S., Beard, J. S., Brunelli, D., Charney, A. B., Christie, D. M., Collins, J., Delacour, A. G., Delius, H., Drouin, M., Einaudi, F., Escartìn, J., Frost, B. R., Früh-Green, G. L., Fryer, P. B., Gee, J. S., Godard, M., Grimes, C. B., Halfpenny, A., Hansen, H. E., Harris, A. C., Tamura, A., Hayman, N. W., Hellebrand, E., Hirose, T., Hirth, J. G., Ishimaru, S., Johnson, K. T. M., Karner, G. D., Linek, M., MacLeod, C. J., Maeda, J., Mason, O. U., McCaig, A. M., Michibayashi, K., Morris, A., Nakagawa, T., Nozaka, T., Rosner, M., Searle, R. C., Suhr, G., Tominaga, M., von der Handt, A., Yamasaki, T. & Zhao, X. (2011). Drilling constraints on lithospheric accretion and evolution at Atlantis Massif, Mid-Atlantic Ridge 30°N. *Journal of Geophysical Research*, **116**, B07103, doi: 10.1029/2010JB007931.

Bloomer, S. H., Meyer, P. S., Dick, H. J. B., Ozawa, K. & Natland, J. H. (1991). Textural and mineralogic variations in gabbroic rocks from Hole 735B. In: Von Herzen, R.P., Robinson, P.T., et al. (Eds.), *Proceedings ODP, Scientific Results*. Ocean Drilling Program, College Station, TX, **118**, 21-39.

Bonatti, E. (1978). Vertical tectonism in oceanic fracture zones. *Earth and Planetary Science Letters*, **37**, 369–379.

Bonatti, E., Ligi, M., Gasperini, L., Peyve, A., Raznitsin, Y. & Chen, Y. J. (1994). Transform migration and vertical tectonics at the Romanche fracture zone, Equatorial Atlantic. *Journal of Geophysical Research*, **99**, 21779-21802.

Bonatti, E., Ligi, M., Borsetti, A. M., Gasperini, L., Negri, A. & Sartori, R. (1996a). Lower Cretaceous deposits trapped near the Mid-Atlantic Ridge and the opening of the equatorial Atlantic. *Nature*, **380**, 518–520.

Bonatti, E., Ligi, M., Carrara, G. et al. (1996b). Diffuse impact of the Mid Atlantic Ridge with the Romanche transform: an Ultracold Ridge/Transform Intersection. *Journal of Geophysical Research*, **101**, 8043-8054.

Bonatti, E., Brunelli, D., Fabretti, P., Ligi, M., Asunta Portaro, R. & Seyler, M. (2001). Steady-state creation of crust-free lithosphere at cold spots in mid-ocean ridges. *Geology*, **29**, 979-982.

Bonatti, E., Ligi, M., Brunelli, D., Cipriani, A., Fabretti, P., Ferrante, V., Gasperini, L. & Ottolini, L. (2003). Mantle thermal pulses below the Mid-Atlantic Ridge and temporal variations in the formation of oceanic lithosphere. *Nature*, **423**, 499–505, doi: 10.1038/nature01594.

Bonatti E., Brunelli D., Buck W. R., Cipriani, A., Fabretti, P., Ferrante, V., Gasperini, L. & Ligi, M. (2005). Flexural uplift of a lithospheric slab near the Vema transform (Central Atlantic): Timing and mechanism. *Earth and Planetary Science Letters*, **240**, 642-655.

Bohrson, W. A., Spera, F. J., Ghiorso, M. S., Brown, G. A., Creamer, J. B. & Mayfield, A. (2014). Thermodynamic model for energy-constrained open system evolution of crustal magma bodies undergoing simultaneous recharge, assimilation and crystallization: the magma chamber simulator. *Journal of Petrology*, **55**, 1685–1717, doi: 10.1093/petrology/egu036.

Bohrson, W. A., Spera, F. J., Heinonen, J. S., Brown, G. A., Scruggs, M. A., Adams, J. V., Takach, M. K., Zeff, G. & Suikkanen, E. (2020). Diagnosing open-system magmatic processes using the Magma Chamber Simulator (MCS): part I-major elements and phase equilibria. *Contributions to Mineralogy and Petrology*, **175**, 104, doi: 10.1007/s00410-020-01722-z.

Boschi, C., Früh-Green, G. L., Delacour, A., Karson, J. A. & Kelley, D. S. (2006). Mass transfer and fluid flow during detachment faulting and development of an oceanic core complex, Atlantis Massif (MAR 30°N). *Geochemistry, Geophysics, Geosystems*, **7**, Q01004, doi: 10.1029/2005GC001074.

Botcharnikov, R. E., Almeev, R., Koepke, J. & Holtz, F. (2008). Phase relations and liquid lines of descent in hydrous ferrobasalt - Implications for the Skaergaard intrusion and Columbia River flood basalts. *Journal of Petrology*, **49**, 1687–1727, doi: 10.1093/petrology/egn043.

Boulanger, M., France, L., Deans, J., Ferrando, C., Lissenberg, C. J. & von der Handt, A. (2020). Magma reservoir formation and evolution at a slow-spreading center (Atlantis Bank, Southwest Indian Ridge). *Frontiers in Earth Sciences*, **8**, 554598, doi:10.3389/feart.2020.554598.

Bown, J. W. & White, R. S. (1994). Variation with spreading rate of oceanic crustal thickness and geochemistry. *Earth and Planetary Science Letters*, **121**, 435-449, doi: 10.1016/0012-821X(94)90082-5.

Brunelli, D., Sanfilippo, A., Bonatti, E, Skolotnev, S., Escartin, J., Ligi, M., Ballabio, G. & Cipriani, A. (2020). Origin of oceanic ferrodiorites by injection of nelsonitic melts in gabbros at the Vema Lithospheric Section, Mid-Atlantic Ridge. *Lithos*, **368-369**, 105589, doi: 10.1016/j.lithos.2020.105589.

Buck, W. R., Lavier, L. L. & Poliakov, A. N. B. (2005). Modes of faulting at mid-ocean ridges. *Nature*, **434**, 719-723, doi: 10.1038/nature03358.

837 Cande, S. C., LaBreque, J. L. & Haxby, W. F. (1988). Plate kinematics of the south Atlantic, chron
838 C34 to the present. *Journal of Geophysical Research*, **93**, 13479-13492.

839 Cann, J. R., Blackman, D. K., Smith, D. K., McAllister, E., Janssen, B., Mello, S., & Pascoe, A. R.,
840 (1997). Corrugated slip surfaces formed at ridge-transform intersections on the Mid-Atlantic
841 Ridge. *Nature*, **385**, 329-332, doi: 10.1038/385329a0.

842 Cannat, M., Mamaloukas-Frangoulis, V., Auzende, J. M., Bideau, D., Bonatti, E., Honnorez, J.,
843 Lagabrielle, Y., Malavieille, J. & Mevel, C. (1991). A geological cross-section of the Vema
844 fracture zone transverse ridge, Atlantic Ocean. *Journal of Geodynamics*, **13**, 97-117, doi:
845 10.1016/0264-3707(91)90034-C.

846 Cannat, M., Sauter, D., Mendel, V., Ruellan, E., Okino, K., Escartin, J., Combier, V. & Baala, M.
847 (2006). Modes of seafloor generation at a melt-poor ultraslow-spreading ridge. *Geology*, **34**, 605-
848 608, doi: 10.1130/G22486.1.

849 Cannat, M., Sauter, D., Lavier, L., Bickert, M., Momoh, E. & Leroy, S. (2019). On spreading modes
850 and magma supply at slow and ultraslow mid-ocean ridges. *Earth and Planetary Science Letters*,
851 **519**, 223-233, doi: 10.1016/j.epsl.2019.05.012.

852 Carbotte, S. & Scheirer, D. S. (2004). Variability of ocean crustal structure created along the global
853 Mid-Ocean Ridge. In: Davis, E. E. & Elderfield, H. (eds.) *Hydrogeology of the oceanic*
854 *lithosphere.* Cambridge University Press, Cambridge, pp 59–107

855 Chen, Y. J. (1992). Oceanic crustal thickness versus spreading rate. *Geophysical Research Letters*,
856 **19**, 753-756, doi: 10.1029/92GL00161.

857 Cipriani, A., Bonatti, E., Brunelli, D. & Ligi, M. (2009). 26 million years of mantle upwelling below
858 a segment of the Mid Atlantic Ridge: The Vema Lithospheric Section revisited. *Earth ad*
859 *Planetary Science Letters*, **285**, 87-95, doi: 10.1016/j.epsl.2009.05.046.

860 Collier, M. L. & Kelemen, P. B. (2010). The case for reactive crystallization at mid-ocean ridges.
861 *Journal of Petrology*, **51**, 1913-1940, doi: 10.1093/petrology/egq043.

862 Coogan, L. A., Saunders, A. D., Kempton, P. D. & Norry, M. J. (2000). Evidence from oceanic
863 gabbros for porous melt migration within a crystal mush beneath the Mid-Atlantic Ridge.
864 *Geochemistry, Geophysics, Geosystems*, **1**, 2000GC000072, doi: 10.1029/2000GC000072.

865 Coogan, L. A., Gillis, K. M., MacLeod, C. J., Thompson, G. M. & Hékinian, R. (2002). Petrology
866 and geochemistry of the lower ocean crust formed at the East Pacific Rise and exposed at Hess

867 Deep: A synthesis and new results. *Geochemistry, Geophysics, Geosystems*, **3**, 8604, doi:
868 10.1029/2001GC000230.

869 Coogan, L. A & O'Hara, M. J. (2015). MORB differentiation: In situ crystallization in replenished-
870 tapped magma chambers. *Geochimica et Cosmochimica Acta*, **158**, 147-161, doi:
871 10.1016/j.gca.2015.03.010.

872 Costa, F., Shea, T. & Ubide, T. (2020). Diffusion chronometry and the timescales of magmatic
873 processes. *Nature Reviews*, **1**, 201-214, doi: 10.1038/s43017-020-0038-x.

874 DePaolo, D. J. (1981). Trace element and isotopic effects of combined wall-rock assimilation and
875 fractional crystallization. *Earth and Planetary Science Letters*, **53**, 189–202, doi: 10.1016/0012-
876 821x(81)90153-9.

877 Dick, H. J. B. & Natland, J. H. (1996). Late-stage melt evolution and transport in the shallow mantle
878 beneath the East Pacific Rise. In: Mével C., Gillis K. M., Allan J. F., Meyer P. S. (eds.)
879 *Proceedings of the Ocean Drilling Program, Scientific Results*, **147**, 103-134, doi:
880 10.2973/odp.proc.sr.147.007.

881 Dick, H. J. B., Natland, J. H., Alt, J. C., Bach, W., Bideau, D., Gee, J. S., Haggas, S., Hertogen, J. G.
882 H., Hirth, G., Holm, P. M., Ildefonse, B., Iturrino, G. J., John, B. E., Kelley, D. S., Kikawa, E.,
883 Kingdon, A., LeRoux, P. J., Maeda, J., Meyer, P. S., Miller, D. J., Naslund, H. R., Niu, Y. -L.,
884 Robinson, P. T., Snow, J., Stephen, R. A., Trimby, P. W., Worm, H. -U. & Yoshinobu, A. (2000).
885 A long in situ section of the lower ocean crust: results of ODP Leg 176 drilling at the Southwest
886 Indian Ridge. *Earth and Planetary Science Letters*, **179**, 31–51, doi: 10.1016/s0012-
887 821x(00)00102-3.

888 Dick, H. J. B., Ozawa, K., Meyer, P. S., Niu, Y., Robinson, P. T., Constantin, M., Hebert, R., Maeda,
889 J., Natland, J. H., Hirth, J. G. & Mackie, S. M. (2002). Primary silicate mineral chemistry of a
890 1.5-km section of very slow spreading lower ocean crust: ODP hole 735B, southwest Indian ridge.
891 In: Natland, J. H., Dick, H. J. B., Miller, D. J. and Von Herzen, R. P. (eds) *Proceedings of the*
892 *Ocean Drilling Program, Scientific Results*, Vol. **176**. College Station, TX: Ocean Drilling
893 Program, pp. 1–61.

894 Dick, H. J. B., Natland, J. H. & Ildefonse, B. (2006). Past and future impact of deep drilling in the
895 oceanic crust and mantle. *Oceanography*, **19**, 72-80.

Dick, H. J. B., Tivey, M. A. & Tucholke, B. E. (2008). Plutonic foundation of a slow-spreading ridge segment: Oceanic core complex at Kane Megamullion, 23°30'N, 45°20'W. *Geochemistry, Geophysics, Geosystems*, **9**, Q05014, doi: 10.1029/2007GC001645.

Dick, H. J. B, Lissenberg, C. J. & Warren, J. M. (2010). Mantle melting melt transport, and delivery beneath a slow-spreading ridge: the paleo-MAR from 23°15′N to 23°45′N. *Journal of Petrology*, **51**, 425–467, doi: 10.1093/petrology/egp088.

Dick, H. J. B., Kvassnes, A. J. S., Robinson, P. T., MacLeod, C. J. & Kinoshita, H. (2019). The Atlantis Bank Gabbro Massif, Southwest Indian Ridge. *Progress in Earth and Planetary Science*, **6**, 64, doi: 10.1186/s40645-019-0307-9.

Dijkstra, A. H., Barth, M. G., Drury, M. R., Mason, P. R. D. & Vissers, R. L. M. (2003). Diffuse porous melt flow and melt-rock reaction in the mantle lithosphere at a slow-spreading ridge: a structural petrology and LA-ICP-MS study of the Othris peridotite massif (Greece). *Geochemistry, Geophysics, Geosystems*, **4**, 8613, doi: 10.1029/2001GC000278.

Drouin, M., Godard, M., Ildefonse, B., Bruguier, O. & Garrido, C. (2009). Geochemical and petrographic evidence for magmatic impregnation in the oceanic lithosphere at Atlantis Massif, Mid-Atlantic Ridge (IODP Hole U1309D, 30°N). *Chemical Geology*, **264**, 71–88, doi: 10.1016/j.chemgeo.2009.02.013.

Elthon, D., Stewart, M. & Ross, K. D. (1992). Compositional trends of minerals in oceanic cumulates. *Journal of Geophysical Research*, **97**, 5189-5199, doi: 10.1029/92JB01187.

Feig, S., Koepke, J. & Snow, J. (2006). Effect of water on tholeiitic basalt phase equilibria: an experimental study under oxidizing conditions. *Contributions to Mineralogy and Petrology*, **152**, 611–638, doi: 10.1007/s00410-006-0123-2.

Ferrando, C., Godard, M., Ildefonse, B. & Rampone, E. (2018). Melt transport and mantle assimilation at Atlantis Massif (IODP Site U1309): constraints from geochemical modelling. *Lithos*, **323**, 24–43, doi: 10.1016/j.lithos.2018.01.012.

Ferrando, C., France, L., Basch, V., Sanfilippo, A., Tribuzio, R. & Boulanger, M. (2021a). Grain size variations record segregation of residual melts in slow-spreading oceanic crust (Atlantis Bank, 57°E Southwest Indian Ridge). *Journal of Geophysical Research: Solid Earth*, **126**, e2020JB020997, doi: 10.1029/2020JB020997.

Ferrando, C., Basch, V., Ildefonse, B., Deans, J., Sanfilippo, A., Barou, F. & France, L. (2021b). Role of compaction in melt extraction and accumulation at a slow spreading center: Microstructures of

olivine gabbros from the Atlantis Bank (IODP Hole U1473A, SWIR). *Tectonophysics*, **815**, 229001, doi: 10.1016/j.tecto.2021.229001.

Fox, P. J. & Gallo D. G. (1984). A tectonic model for ridge-transform-ridge plate boundaries: Implications for the structure of oceanic lithosphere. *Tectonophysics*, **104**, 205-242.

Gardner, R. L., Piazolo, S., Daczko, N. R. & Trimby, P. (2020). Microstructures reveal multistage melt present strain localisation in mid-ocean gabbros. *Lithos*, **366-367**, 105572, doi: 10.1016/j.lithos.2020.105572.

Gillis, K. M., Snow, J. E., et al. (2014). Primitive layered gabbros from fast-spreading lower oceanic crust. *Nature*, **505**, 204-211, doi: 10.1038/nature12778.

Godard, M., Awaji, S., Hansen, H., Hellebrand, E., Brunelli, D., Johnson, K., et al. (2009). Geochemistry of a long in-situ section of intrusive slow-spread oceanic lithosphere: Results from IODP Site U1309 (Atlantis Massif, 30°N Mid-Atlantic-Ridge). *Earth and Planetary Science Letters*, **279**, 110–122, doi: 10.1016/j.epsl.2008.12.034.

Grove, T. L., Kinzler, R. J. & Bryan, W. B. (1992). Fractionation of Mid-Ocean Ridge Basalt (MORB). In: Phipps Morgan, J., Blackman, D. K. & Sinton, J. M. (Eds.) Mantle Flow and melt generation at mid-ocean ridges, *Geophysical Monograph Series*, **71**, 281-310, doi: 10.1029/GM071p0281.

Ghiorso, M. S. & Sack, O. (1995). Chemical mass transfer in magmatic processes. IV. A revised and internally consistent thermodynamic model for the interpolation and extrapolation of liquid-solid equilibria in magmatic systems at elevated temperatures and pressures. *Contributions to Mineralogy and Petrology*, **119**, 197–212, doi:10.1007/BF00307281.

Heinonen, J. S., Bohrson, W. A., Spera, F. J., Brown, G. A., Scruggs, M. & Adams, J. (2020). Diagnosing open-system magmatic processes using the Magma Chamber Simulator (MCS): part II—trace elements and isotopes. *Contributions to Mineralogy and Petrology*, **175**, 105, doi: 10.1007/s00410-020-01718-9

Hekinian, R., Juteau, T., Gràcia, E. Sichler, B., Sichel, S., Udintsev, G., Apprioual, R. & Ligi, M. (2000). Submersible observations of Equatorial Atlantic mantle: the St. Paul Fracture Zone region. *Marine Geophysical Researches*, **21**, 529, doi: 10.1023/A:1004819701870.

Hooft, E. E. E., Detrick, R. S., Toomey, D. R., Collins, J. A. & Lin, J. (2000). Crustal thickness and structure along three contrasting spreading segments of the Mid-Atlantic Ridge, 33.5°–35°N, *Journal of Geophysical. Research*, **105**, 8205-8226, doi:10.1029/1999JB900442.

Karson, J. A., Früh-Green, G. L., Kelley, D. S., Williams, E. A., Yoerger, D. R. & Jakuba, M. (2006). Detachment shear zone of the Atlantis Massif core complex, Mid-Atlantic Ridge, 30°N. *Geochemistry, Geophysics, Geosystems*, **7**, Q06016, doi: 10.1029/2005GC001109.

Klein, E. M. & Langmuir, C. H. (1987). Global correlations of ocean ridge basalt chemistry with axial depth and crustal thickness. *Journal of Geophysical Research*, **92**, 8089-8115.

Koepke, J., Botcharnikov, R. E. & Natland, J. H. (2018). Crystallization of late-stage MORB under varying water activities and redox conditions: Implications for the formation of highly evolved lavas and oxide gabbro in the ocean crust. *Lithos*, **323**, 58-77, doi: 10.1016/j.lithos.2018.10.001.

Langmuir, C. H. & Forsyth, D. W. (2007). Mantle melting beneath mid-ocean ridges. *Oceanography* **20**, 78–89.

Leake, B. E., Woolley, A. R., Arps, C. E. S., Birch, W. D., Gilbert, M. C., Grice, J. D., et al. (1997). Nomenclature of amphiboles: Report of the subcommittee on amphiboles of the International Mineralogical Association Commission on New Minerals and Mineral Names. *The Canadian Mineralogist*, **35**, 219–246.

Liang, Y. (2003). Kinetics of crystal–melt reaction in partially molten silicates: 1. Grain scale processes. *Geochemistry, Geophysics, Geosystems*, **4**, 1045, doi:10.1029/2002GC000375.

Ligi, M., Bonatti, E., Gasperini, L. & Poliakov, A. N. B. (2002). Oceanic broad multifault transform plate boundaries. *Geology*, **30**, 11-14.

Ligi, M., Bonatti, E., Cipriani, A. & Ottolini, L. (2005). Water-rich basalts at mid-ocean-ridge cold spots. *Nature*, **434**: 66-69.

Lissenberg, C. J. & Dick, H. J. B. (2008). Melt–rock reaction in the lower oceanic crust and its implications for the genesis of mid-ocean ridge basalt. *Earth and Planetary Science Letters*, **271**, 311–325, doi: 10.1016/j.epsl.2008.04.023.

Lissenberg, C. J., MacLeod, C. J., Howard, K. A. & Godard, M. (2013). Pervasive reactive melt migration through fast-spreading lower oceanic crust (Hess Deep, equatorial Pacific Ocean). *Earth and Planetary Science Letters*, **361**, 436-447, doi: 10.1016/j.epsl.2012.11.012.

Lissenberg, C. J. & MacLeod, C. J. (2016). A reactive porous flow control on mid-ocean ridge magmatic evolution. *Journal of Petrology*, **57**, 2195-2220, doi: 10.1093/petrology/egw074.

Lissenberg, C. J., MacLeod, C. J. & Bennett, E. N. (2019). Consequences of a crystal mush-dominated magma plumbing system: a mid-ocean ridge perspective. *Philosophical Transactions of the Royal Society A.*, **377**, 20180014, doi: 10.1098/rsta.2018.0014.

Liu, T., Wu, F.-Y., Liu, C.-Z., Tribuzio, R., Ji, W.-B., Zhang, C., Xu, Y. & Zhang, W.-Q. (2018). Variably evolved gabbroic intrusions within the Xigaze ophiolite (Tibet): new insights into the origin of ophiolite diversity. *Contributions to Mineralogy and Petrology*, **173**, 91, doi: 10.1007/s00410-018-1518-6.

Luo, Y., Lin, J., Zhang, F. & Wei, M. (2021). Spreading rate dependance of morphological characteristics in global oceanic transform faults. *Acta Oceanologica Sinica*, **40**, 39-64, doi: 10.1007/s13131-021-1722-5.

MacLeod, C. J., Dick, H. J. B., Blum, P. et al. (2017). Expedition 360 summary. In: MacLeod, C. J., Dick, H. J. B., Blum, P. and the Expedition 360 Scientists (Eds.), Southwest Indian Ridge lower crust and Moho. *Proceedings of the International Ocean Discovery Program*, Vol. **360**: 1-267, doi: 10.14379/iodp.proc.360.103.2017.

Maia, M., Sichel, S., Briais, A. et al. (2016). Extreme mantle uplift and exhumation along a transpressive transform fault. *Nature Geoscience*, **9**, 619-624, doi: 10.1038/NGEO2759.

Maia, M. (2019). Chapter 3 - Topographic and Morphologic Evidences of Deformation at Oceanic Transform Faults: Far-Field and Local-Field Stresses. In: Duarte, J. C. (eds) *Transform Plate Boundaries and Fracture Zones*, 61-87, doi: 10.1016/B978-0-12-812064-4.00003-7.

Mével, C., Cannat, M., Gente, P., Marion, E., Auzende, J. M. & Karson, J. A. (1991) Emplacement of deep crustal and mantle rocks on the west median valley wall of the MARK area (MAR, 23°N). *Tectonophysics*, **190**, 31-53, doi: 10.1016/0040-1951(91)90353-T.

Miller, D. J., Abratis, M., Christie, D., Drouin, M., Godard, M., Ildefonse, B., Maeda, J., Weinsteiger, A., Yamasaki, T., Suzuki, Y., Niino, A., Sato, Y. & Takeda, F. (2009). Data report: microprobe analyses of primary mineral phases from site U1309, Atlantis Massif, IODP Expedition 304/305. In: Blackman, D. K., Ildefonse, B., John, B. E., Ohara, Y., Miller, D. J., MacLeod, C. J. & the Expedition 304/305 Scientists (eds.) *Proceedings of the International Ocean Drilling Program*, **304/305**. College Station, TX: Integrated Ocean Drilling Program, p. 4.

Natland, J. H., Meyer, P. S., Dick, H. J. B. & Bloomer, S. H. (1991). Magmatic oxides and sulfides in gabbroic rocks from ODP Hole 735B and the later development of the liquid line of descent.

In: Von Herzen, R.P., Robinson, P.T., et al. (Eds.), *Proceedings ODP, Scientific Results. Ocean Drilling Program, College Station, TX*, **118**, 75–111, doi: 10.2973/odp.proc.sr.118.163.1991.

Niu, Y. & Hékinian, R. (1997). Spreading-rate dependence of the extent of mantle melting beneath ocean ridges. *Nature*, **385**, 326–329

Niu, Y. (1997). Mantle melting and melt extraction processes beneath ocean ridges: evidence from abyssal peridotites. *Journal of Petrology*, **38**, 1047–1074.

Niu, Y. (2021). Lithosphere thickness controls the extent of mantle melting, depth of melt extraction and basalt compositions in all tectonic settings on Earth – A review and new perspectives. *Earth-Science Reviews*, **217**: 103614, doi: 10.1016/j.earscirev.2021.103614.

Olive, J.-A. & Dublanchet, P. (2020). Controls on the magmatic fraction of extension at mid-ocean ridges. *Earth and Planetary Science Letters*, **549**, 116541, doi: 10.1016/j.epsl.2020.116541.

Ozawa, K., Meyer, P. S. & Bloomer, S. H. (1991). Mineralogy and textures of iron-titanium-oxide gabbros from hole 735B. In: Von Herzen, R.P., Robinson, P.T., et al. (Eds.), *Proceedings ODP, Scientific Results. Ocean Drilling Program, College Station, TX*, **118**, 41–73, doi: 10.2973/odp.proc.sr.118.125.1991.

Parmentier, E. M. & Phipps Morgan, J. (1990). Spreading rate dependence of three-dimensional structure in oceanic spreading centres. *Nature*, **348**, 325-328.

Pushcharovsky, Yu. M., Raznitsin, Yu. N., Mazarovich, A. O. et al. (1991). Structure of the Doldrums fracture zone Central Atlantic. *M. Nauka*, 224 pp. (in Russian).

Pushcharovsky, Yu. M., Raznitsin, Yu. N., Mazarovich, A.O., Skolotnev, S. G., Kepezinskas, P. K., Tyrko, N. N., Peyve, A. A. & Dmitriev, D. A. (1992). Fracture zones Arkhangelsky, Doldrums and Vernadsky in the Central Atlantic: structure and rocks composition. *Geotectonika*, **6**, 63-79 (in Russian).

Rampone, E., Borghini, G. & Basch, V. (2020). Melt migration and melt–rock reaction in the Alpine-Apennine peridotites: insights on mantle dynamics in extending lithosphere. *Geoscience Frontiers*, **11**, 151-166, doi: 10.1016/j.gsf.2018.11.001.

Sandwell, D. T. & Smith, W. H. F. (1997). Marine gravity anomaly from Geasat and ERS-1 satellite altimetry: *Journal of Geophysical Research*, **102**, 10039-10054.

1044 Sanfilippo, A., Tribuzio, R. & Tiepolo, M. (2014). Mantle-crust interactions in the oceanic
1045 lithosphere: Constraints from minor and trace elements in olivine. *Geochimica et Cosmochimica*
1046 *Acta*, **141**, 423-439, doi: 10.1016/j.gca.2014.06.012.

1047 Sanfilippo, A., Dick, H. J. B., Ohara, Y. & Tiepolo, M. (2016). New insights on the origin of
1048 troctolites from the breakaway area of the Godzilla Megamullion (Parece Vela back-arc basin):
1049 The role of melt-mantle interaction on the composition of the lower crust. *Island Arc*, **25**, 220-
1050 234, doi: 10.1111/iar.12137.

1051 Sanfilippo, A., Dick, H. J. B., Marschall, H. R., Lissenberg, C. J. & Urann, B. (2019). Emplacement
1052 and high-temperature evolution of gabbros of the 16.5°N oceanic core complexes (Mid-Atlantic
1053 Ridge): Insights into the compositional variability of the lower oceanic crust. *Geochemistry,*
1054 *Geophysics, Geosystems*, **20**, 46-66, doi: 10.1029/2018GC007512.

1055 Sanfilippo, A., MacLeod, C.J., Tribuzio, R., Lissenberg, C.J. & Zanetti, A. (2020). Early-stage melt-
1056 rock reaction in a cooling crystal mush beneath a slow-spreading mid-ocean ridge (IODP Hole
1057 U1473A, Atlantis Bank, Southwest Indian Ridge). *Frontiers in Earth Science*, **8**, 579138, doi:
1058 10.3389/feart.2020.579138.

1059 Sani, C., Sanfilippo, A., Ferrando, C., Peyve, A. A., Skolotnev, S. G., Muccini, F., Zanetti, A., Basch,
1060 V., Palmiotto, C., Bonatti, E. & Ligi, M. (2020). Ultra-depleted melt refertilization of mantle
1061 peridotites in a large intra-transform domain (Doldrums Fracture Zone; 7-8°N, Mid Atlantic
1062 Ridge). *Lithos*, **374-375**, 105698, doi: 10.1016/j.lithos.2020.105698.

1063 Schilling, J. G., Ruppel, C., Davis, A. N., McCully, B., Tighe, S. A., Kingsley, R. H. & Lin, J. (1995).
1064 Thermal structure of the mantle beneath the equatorial mid-Atlantic ridge - Inferences from the
1065 spatial variation of dredged basalt glass compositions. *Journal of Geophysical Research*, **100**,
1066 10057–10076.

1067 Searle, R. C., Thomas, M. V. & Jones, E. J. W. (1994). Morphology and tectonics of the Romanche
1068 Transform and its environs. *Marine Geophysical Researches*, **16**, 427-453.

1069 Skolotnev, S. G., Sanfilippo, A., Peyve, A. A., Muccini, F., Sokolov, S. Y., Sani, C., Dobroliubova,
1070 K. O., Ferrando, C., Chamov, N. P., Palmiotto, C., Pertsev, A. N., Bonatti, E., Cuffaro, M.,
1071 Gryaznova, A. C., Sholukhov, K. N., Bich, A. S. & Ligi, M. (2020). Large-scale structure of the
1072 Doldrums multi-fault transform system (7-8°N Equatorial Atlantic): preliminary results from the
1073 45th expedition of the R/V A.N. Strakhov. *Ofioliti*, **45**: 25-41.

1074 Suhr, G., Hellebrand, E., Johnson, K. & Brunelli, D. (2008). Stacked gabbro units and intervening
1075 mantle: a detailed look at a section of IODP Leg 305, Hole U1309D. *Geochemistry, Geophysics,*
1076 *Geosystems*, **9**, doi: 10.1029/2008GC002012.

1077 Sun, S. -S. & McDonough, W. F. (1989). Chemical and isotopic systematics of oceanic basalts:
1078 implications for mantle composition and processes. In: Saunders AD, Norry MJ (eds) Magmatism
1079 in the ocean basins, Vol **42**. *Geological Society, London*, pp 313–345 (Special Publications).

1080 Takeuchi, C. S., Sclater, J. G., Grindlay, N. R., Madsen, J. A. & Rommevaux-Jestin, C. (2010).
1081 Segment-scale and intrasegment lithospheric thickness and melt variations near the Andrew Bain
1082 megatransform fault and Marion hot spot: Southwest Indian Ridge, 25.5°E-35°E. *Geochemistry,*
1083 *Geophysics, Geosystems*, **11**, Q07012, doi: 10.1029/2010GC003054.

1084 Tribuzio, R., Manatschal, G., Renna, M. R., Ottolini, L. & Zanetti, A. (2020). Tectono-magmatic
1085 interplay and related metasomatism in gabbros of the Chenaillet ophiolite (Western Alps). *Journal*
1086 *of Petrology*, **60**, 2483-2508, doi: 10.1093/petrology/egaa015.

1087 Tucholke, B. E., Behn, M. D., Buck, W. R. & Lin, J. (2008). Role of melt supply in oceanic
1088 detachment faulting and formation of megamullions. *Geology*, **36**, 455-458, doi:
1089 10.1130/G24639A.1

1090 Warren, J. M. & Shimizu, N. (2010). Cryptic variations in abyssal peridotite compositions: evidence
1091 for shallow-level melt infiltration in the oceanic lithosphere. *Journal of Petrology*, **51**: 395–423,
1092 doi: 10.1093/petro logy/egp096.

1093 White, W. M., Klein, E. M. (2014). Composition of the Oceanic crust. In: Turekian, K. & Holland,
1094 H. (eds.) *Treatise on Geochemistry 2nd Edition*, **4**, 457-496, doi: 10.1016/B978-0-08-095975-
1095 7.00315-6

1096 Wilson, J. T. (1965). A new class of faults and their bearing on continental drift. *Nature*, **207**, 343-
1097 347.

1098 Workman, R. K. & Hart, S. R. (2005). Major and trace element composition of the depleted MORB
1099 mantle (DMM). *Earth and Planetary Science Letters*, **231**, 53–72, doi:
1100 10.1016/j.epsl.2004.12.005.

1101 Zellmer, G. F., Sakamoto, N., Matsuda, N., Iizuka, Y., Moebis, A. & Yurimoto, H. (2016). On
1102 progress and rate of the peritectic reaction Fo + SiO_2 → En in natural andesitic arc magmas.
1103 *Geochimica et Cosmochimica Acta*, **185**, 383-393, doi : 10.1016/j.gca.2016.01.005.

Zhang, W. Q., Liu, C. Z., & Dick, H. J. B. (2020). Evidence for multi-stage melt transport in the lower ocean crust: Atlantis Bank gabbroic massif (IODP Hole U1473A, SW Indian Ridge). *Journal of Petrology*, **61**, egaa082, doi: 10.1093/petrology/egaa082.

Zhang, W. Q., Dick, H. J. B., Liu, C. Z., Lin Y. Z. & Angeloni, L. M. (2021). MORB melt transport through Atlantis Bank oceanic batholith (SW Indian Ridge). *Journal of Petrology*, **62**, egab034, doi: 10.1093/petrology/egab034.

FIGURE CAPTIONS

Figure 1: a) Bathymetric map of the Doldrums Megatransform System, combining the data acquired during expedition S45 (see Skolotnev *et al.*, 2020) and the GEBCO bathymetric dataset. Black lines delineate the Mid-Atlantic Ridge and the Intra-Transform Ridge segments, whereas the white lines highlight the active portions of the transform faults. The inset map indicates the location of the studied area in the equatorial Mid-Atlantic Ridge; b) Detailed bathymetric map of the ITR-1. The location of the sampled dredges is indicated by white dots and the proportion of sampled lithologies are represented by pie charts.

Figure 2: a) Detailed bathymetric map of the Peyve Seamount. The locations of the bathymetric profiles A-B and C-D are represented by white lines; b) Profile A-B across the ridge valley and along the Peyve Seamount; c) Profile C-D across the Peyve Seamount and the Vernadsky transform valley; d) Three-dimensional rendering of the bathymetry of Seamount Peyve and associated dredge deployment. The colour scale is the same as the bathymetric map; e) Pie diagrams representing the proportion of all the gabbroic lithotype recovered in the ITR-1 domain and on the Seamount Peyve, redrawn after Skolotnev *et al.* (2020).

Figure 3: Representative photomicrographs of the olivine gabbros and gabbros sampled at Seamount Peyve. The textures are shown in nicols-parallel and crossed-nicols in the left and right column, respectively; a) Olivine gabbro S45-7-2; b) Olivine gabbro S45-7-7; c) Gabbro S45-7-1B. PL = Plane-polarized light; XPL = Crossed-nicols polarized light.

Figure 4: Representative photomicrographs of the orthopyroxene- and oxide-bearing gabbros sampled at Seamount Peyve. The textures are shown in nicols-parallel and crossed-nicols in the left and right column, respectively; a) Gabbronorite S45-7-4B; b) Oxide gabbronorite S45-7-8; c) Oxide gabbro S45-7-6B; d) Oxide gabbro S45-7-6A. PL = Plane-polarized light; XPL = Crossed-nicols polarized light.

Figure 5: Bulk-rock compositions of the different gabbroic lithologies recovered in the studied area. The composition of bulk Seamount Peyve has been calculated as the weighted average of all recovered samples. The compositions of gabbroic rocks recovered at the Atlantis Massif (after Godard *et al.*, 2009) and Atlantis Bank (after Dick *et al.*, 2000) are represented for comparison; a) Mg-value (100x cationic Mg/(Mg+Fe) mol%) vs Ca-value (100x cationic Ca/(Ca+Na) mol%); b) MgO (wt%) vs FeO (wt%). The compositional field of Mid-Atlantic Ridge peridotites is after Godard *et al.* (2009).

Figure 6: Bulk-rock compositions of the different gabbroic lithologies recovered in the studied area. The compositions of gabbroic rocks recovered at the Atlantis Massif (after Godard *et al.*, 2009) and Atlantis Bank (after Dick *et al.*, 2000) are represented for comparison; MgO content (wt%) vs a) SiO_2 (wt%); b) CaO (wt%); c) Al_2O_3 (wt%); d) TiO_2 (wt%); Na_2O (wt%); CaO/Al_2O_3.

Figure 7: Bulk-rock trace element compositions of the different gabbroic lithologies recovered in the studied area; a) C1-chondrite normalized REE patterns of olivine gabbros, gabbros and oxide gabbros; b) C1-chondrite normalized REE patterns of gabbronorites and dolerites; c) Primitive Mantle-normalized trace element pattern of olivine gabbros, gabbros and oxide gabbros; d) Primitive Mantle-normalized trace element pattern of gabbronorites and dolerites. Normalization values after Sun and McDonough (1989).

Figure 8: Mineral major element compositions within the different gabbroic lithologies recovered in the studied area. The compositions of gabbroic rocks recovered at the Atlantis Massif (after Miller *et al.*, 2009) and Atlantis Bank (after Dick *et al.*, 2002) are represented for comparison; a) Clinopyroxene Mg-value vs Al_2O_3; b) Clinopyroxene Mg-value vs TiO_2; c) Mg-value in clinopyroxene vs anorthite content in plagioclase; d) Plagioclase anorthite content vs K_2O; e) Orthopyroxene Mg-value vs Al_2O_3; f) Orthopyroxene Mg-value vs TiO_2.

Figure 9: Mineral trace element compositions within the different gabbroic lithologies recovered in the studied area; C1-chondrite normalized REE patterns and Primitive Mantle-normalized trace element patterns of a-b) Clinopyroxene; c-d) Plagioclase; e-f) Orthopyroxene; g-h) Amphibole. Normalization values after Sun and McDonough (1989).

Figure 10: Representative sketch of the inferred process of lateral differentiation, resulting from the reduced melt productivity in the vicinity of the transform fault. The red box indicates the geological setting of the sketch in Figure 17.

Figure 11: Primitive Mantle-normalized trace element patterns of the melts computed in equilibrium with clinopyroxene from: a) Olivine gabbros, Gabbros and Oxide gabbros; b) Gabbronorites. The trace element patterns of primitive N-MORB melts (after Workman and Hart, 2005) and the basalts sampled at the Seamount Peyve are plotted for comparison. Normalization values are after Sun and McDonough (1989) and the compilation of partition coefficients used for calculating the equilibrium melts is after Basch *et al.* (2018).

Figure 12: Modal contents (vol%) of the cumulate gabbro formed during fractional crystallization of an evolved melt, involving the assimilation of various quantities of a primitive crystal mush (10 vol% olivine, 50 vol% plagioclase, 40 vol% clinopyroxene). The composition of the basalt S45-07-173 has been selected as the starting melt composition. Models were computed using the MELTS thermodynamic software (Ghiorso and Sack, 1995). The different models assume a) Fractional Crystallization (FC); b) FC and concomitant assimilation of 0.5g/°C of cooling; c) FC and concomitant assimilation of 1g/°C of cooling; d) FC and concomitant assimilation of 1.5g/°C of cooling; e) FC and concomitant assimilation of 2g/°C of cooling. The yellow field highlights the appearance of orthopyroxene in the fractionated cumulate gabbro.

Figure 13: Clinopyroxene Y_N vs La_N/Sm_N. Compositional trends represent clinopyroxenes computed in equilibrium with melts residual after the process of Assimilation-Fractional Crystallization (AFC models, using the equation from DePaolo, 1981). Ma/Mc ranges from 0 to 0.9. Each tick along the compositional trends represents a decrease in residual melt mass of 5 vol%. Oxide gabbronorites sampled at the Atlantis Bank are shown for comparison (after Zhang *et al.*, 2020). Normalization values are after Sun and McDonough (1989).

Figure 14: Primitive Mantle-normalized trace element patterns of the melt compositions in equilibrium with clinopyroxenes from Figure 13, compared with patterns of Assimilation-Fractional Crystallization (after De Paolo, 1981) of a basaltic parental composition (S45-7-180) assimilating a primitive crystal mush (10 vol% olivine, 40 vol% clinopyroxene, 50 vol% plagioclase) at variable ratios mass assimilated/mass crystallized; a) Model computed at low assimilated mass (Ma/Mc = 0.3) to reproduce the compositions of the oxide gabbros; b) Model computed at high assimilated mass (Ma/Mc = 0.8) to reproduce the compositions of the gabbronorites. Melt fraction decreases from 100% to 5% of the initial melt mass. Mineral/melt partition coefficients are after Basch *et al.* (2018) and normalization values are after Sun and McDonough (1989).

Figure 15: a) Close-up of the magmatic processes occurring in the vicinity of a cold ridge-transform intersection. A lens of primitive gabbroic crystal mush is invaded by the evolved melts percolating laterally from the central portion of the ridge segment. Reaction between the primitive crystal mush and the evolved melt leads to partial assimilation of the gabbroic mush and to the process modeled in Figures 14, 15 and 16; b) Detail of the local melt hybridization, leading to the formation of replacive lithologies ranging from oxide gabbros to oxide gabbronorites and gabbronorites. Each melt percolation channel is characterized by its intrinsic reactivity towards the primitive gabbroic mush, as a function of the melt composition and temperature. Intensive assimilation (Ma/Mc > 0.7) results in the formation of gabbronorites, whereas weaker assimilation (Ma/Mc < 0.5) leads to the formation of oxide gabbros.

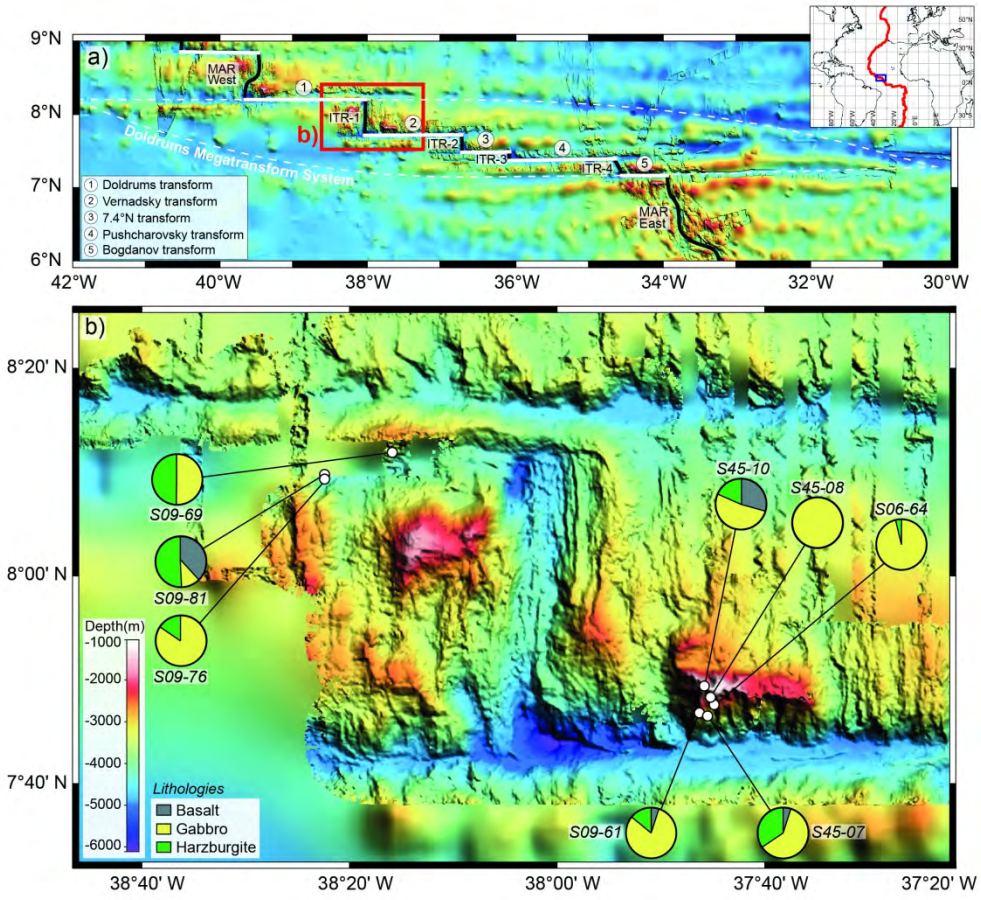

Figure 1: a) Bathymetric map of the Doldrums Megatransform System, combining the data acquired during expedition S45 (see Skolotnev et al., 2020) and the GEBCO bathymetric dataset. Black lines delineate the Mid-Atlantic Ridge and the Intra-Transform Ridge segments, whereas the white lines highlight the active portions of the transform faults. The inset map indicates the location of the studied area in the equatorial Mid-Atlantic Ridge; b) Detailed bathymetric map of the ITR-1. The location of the sampled dredges is indicated by white dots and the proportion of sampled lithologies are represented by pie charts.

213x196mm (300 x 300 DPI)

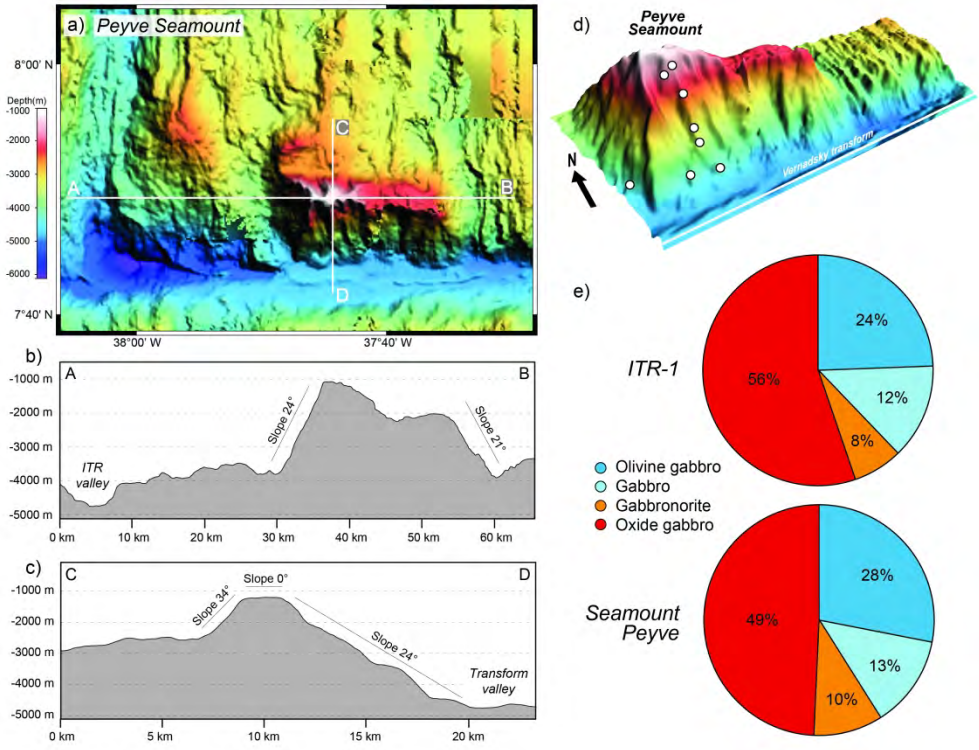

Figure 2: a) Detailed bathymetric map of the Peyve Seamount. The locations of the bathymetric profiles A-B and C-D are represented by white lines; b) Profile A-B across the ridge valley and along the Peyve Seamount; c) Profile C-D across the Peyve Seamount and the Vernadsky transform valley; d) Three-dimensional rendering of the bathymetry of Seamount Peyve and associated dredge deployment. The colour scale is the same as the bathymetric map; e) Pie diagrams representing the proportion of all the gabbroic lithotype recovered in the ITR-1 domain and on the Seamount Peyve, redrawn after Skolotnev et al. (2020).

299x231mm (300 x 300 DPI)

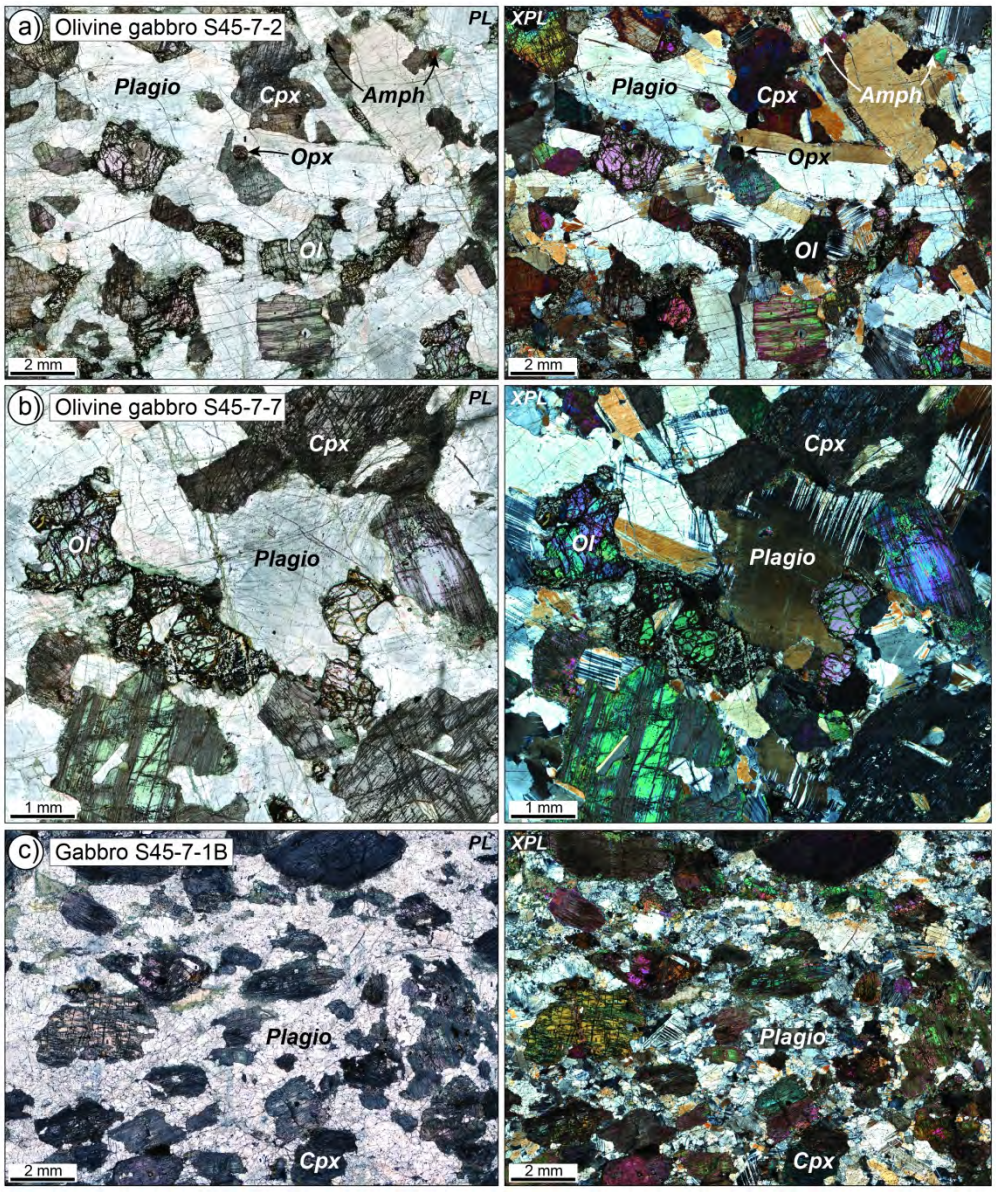

Figure 3: Representative photomicrographs of the olivine gabbros and gabbros sampled at Seamount Peyve. The textures are shown in nicols-parallel and crossed-nicols in the left and right column, respectively; a) Olivine gabbro S45-7-2; b) Olivine gabbro S45-7-7; c) Gabbro S45-7-1B. PL = Plane-polarized light; XPL = Crossed-nicols polarized light.

207x247mm (300 x 300 DPI)

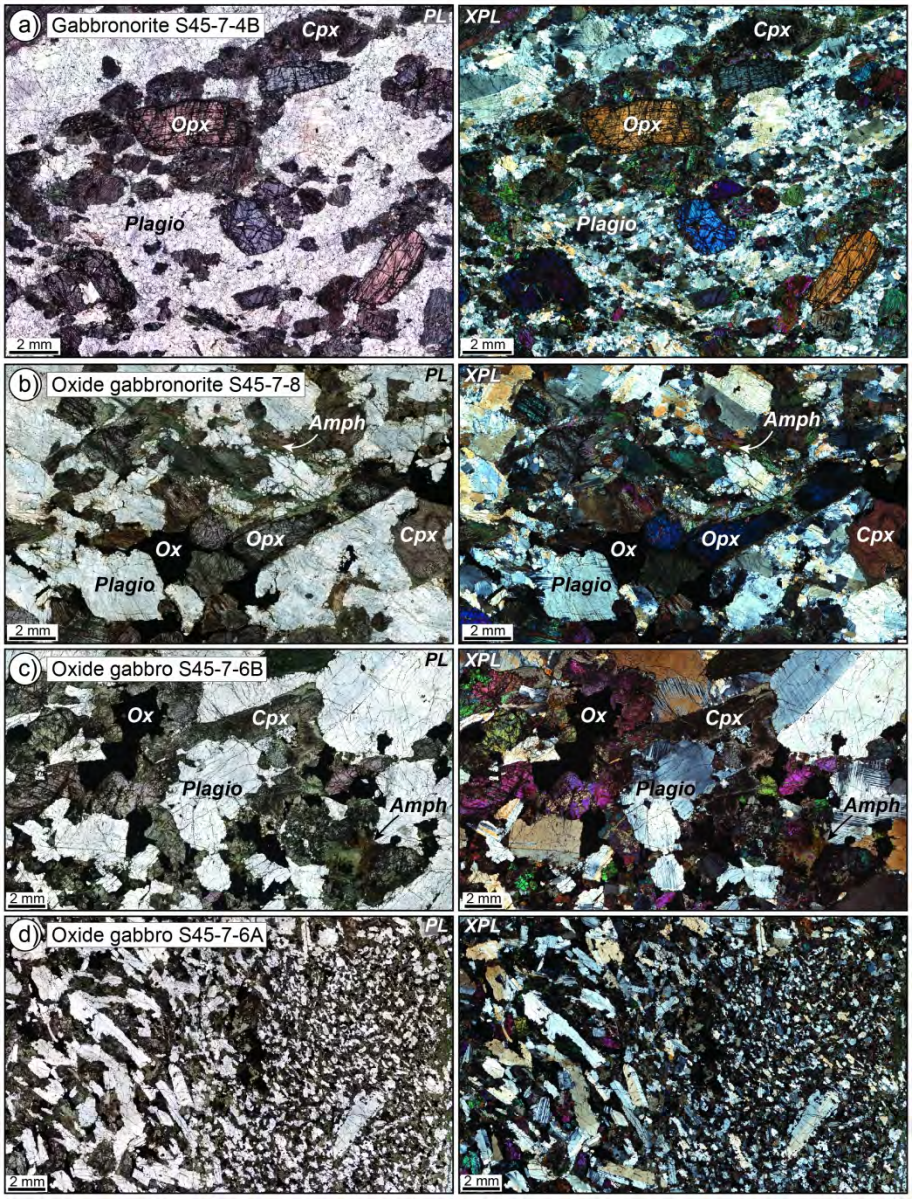

Figure 4: Representative photomicrographs of the orthopyroxene- and oxide-bearing gabbros sampled at Seamount Peyve. The textures are shown in nicols-parallel and crossed-nicols in the left and right column, respectively; a) Gabbronorite S45-7-4B; b) Oxide gabbronorite S45-7-8; c) Oxide gabbro S45-7-6B; d) Oxide gabbro S45-7-6A. PL = Plane-polarized light; XPL = Crossed-nicols polarized light.

207x272mm (300 x 300 DPI)

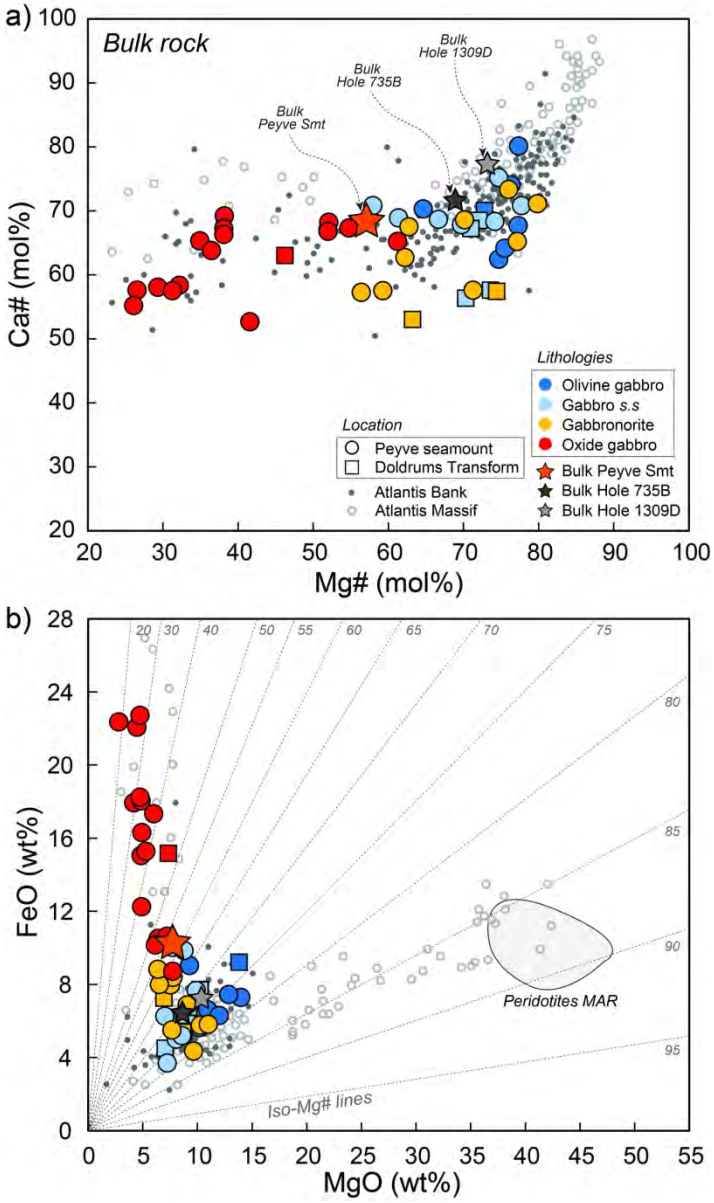

Figure 5: Bulk-rock compositions of the different gabbroic lithologies recovered in the studied area. The composition of bulk Seamount Peyve has been calculated as the weighted average of all recovered samples. The compositions of gabbroic rocks recovered at the Atlantis Massif (after Godard et al., 2009) and Atlantis Bank (after Dick et al., 2000) are represented for comparison; a) Mg-value (100x cationic Mg/(Mg+Fe) mol%) vs Ca-value (100x cationic Ca/(Ca+Na) mol%); b) MgO (wt%) vs FeO (wt%). The compositional field of Mid-Atlantic Ridge peridotites is after Godard et al. (2009).

125x213mm (300 x 300 DPI)

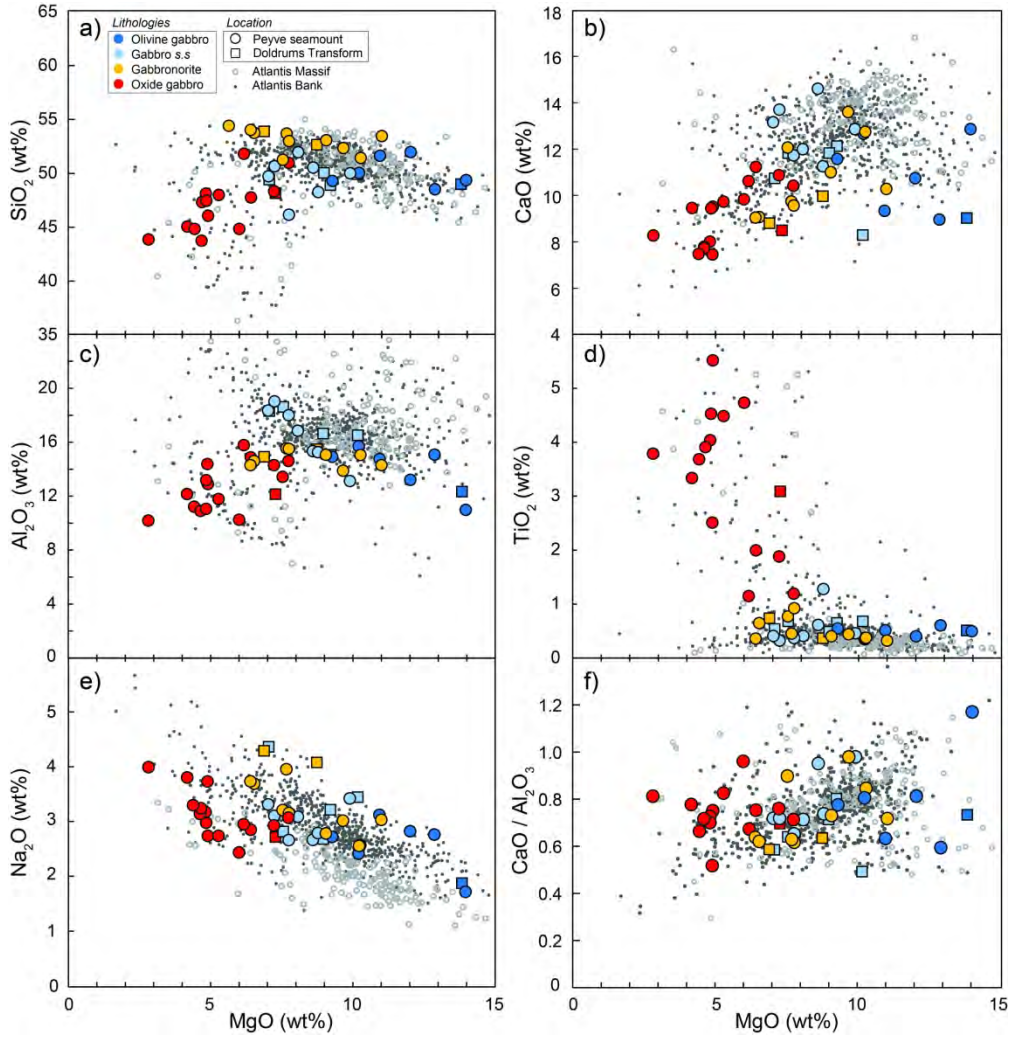

Figure 6: Bulk-rock compositions of the different gabbroic lithologies recovered in the studied area. The compositions of gabbroic rocks recovered at the Atlantis Massif (after Godard et al., 2009) and Atlantis Bank (after Dick et al., 2000) are represented for comparison; MgO content (wt%) vs a) SiO2 (wt%); b) CaO (wt%); c) Al2O3 (wt%); d) TiO2 (wt%); Na2O (wt%); CaO/Al2O3.

202x209mm (300 x 300 DPI)

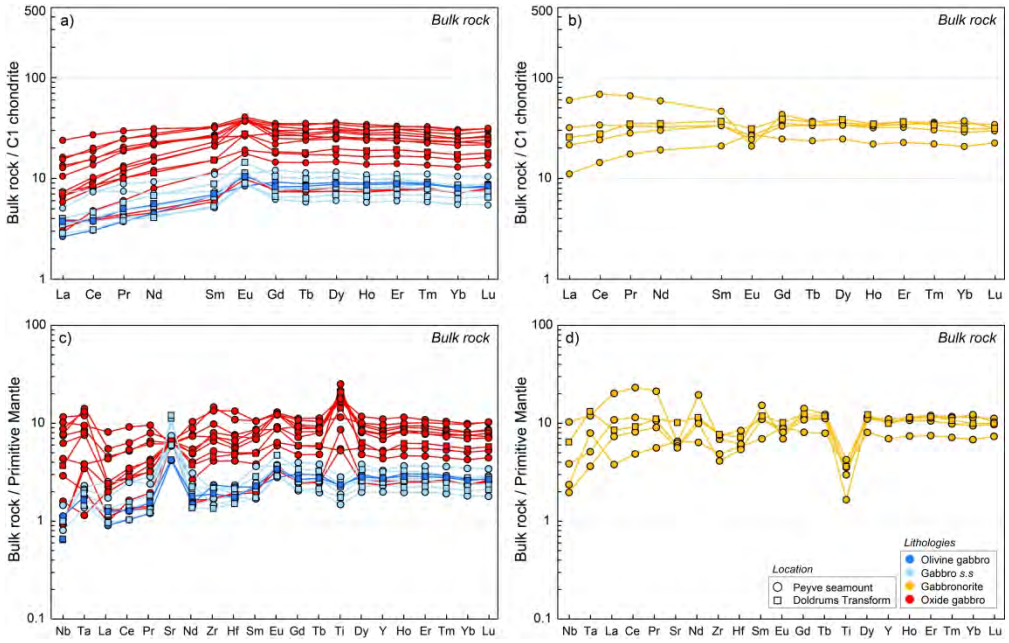

Figure 7: Bulk-rock trace element compositions of the different gabbroic lithologies recovered in the studied area; a) C1-chondrite normalized REE patterns of olivine gabbros, gabbros and oxide gabbros; b) C1-chondrite normalized REE patterns of gabbronorites and dolerites; c) Primitive Mantle-normalized trace element pattern of olivine gabbros, gabbros and oxide gabbros; d) Primitive Mantle-normalized trace element pattern of gabbronorites and dolerites. Normalization values after Sun and McDonough (1989).

298x189mm (300 x 300 DPI)

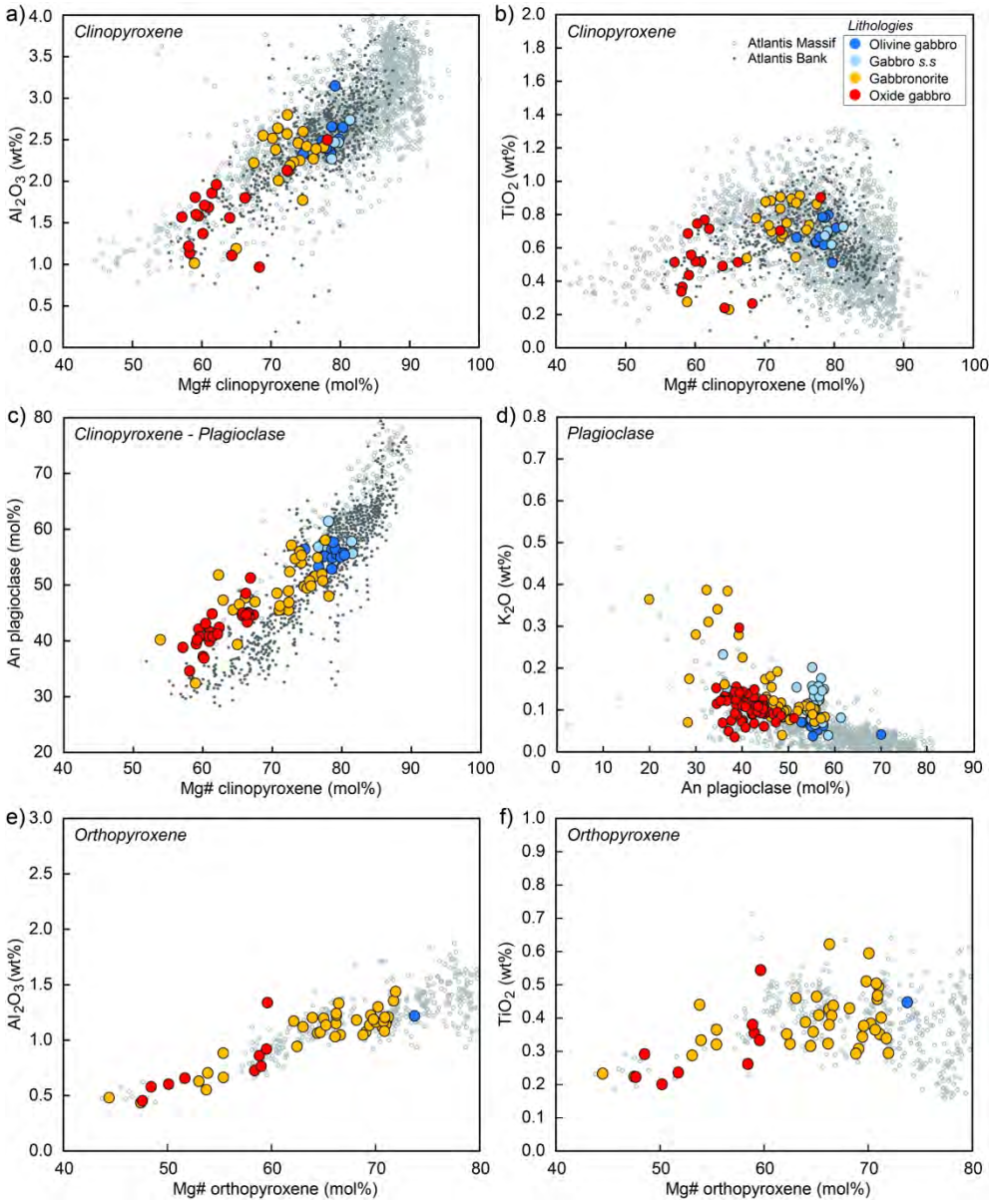

Figure 8: Mineral major element compositions within the different gabbroic lithologies recovered in the studied area. The compositions of gabbroic rocks recovered at the Atlantis Massif (after Miller et al., 2009) and Atlantis Bank (after Dick et al., 2002) are represented for comparison; a) Clinopyroxene Mg-value vs Al2O3; b) Clinopyroxene Mg-value vs TiO2; c) Mg-value in clinopyroxene vs anorthite content in plagioclase; d) Plagioclase anorthite content vs K2O; e) Orthopyroxene Mg-value vs Al2O3; f) Orthopyroxene Mg-value vs TiO2.

204x248mm (300 x 300 DPI)

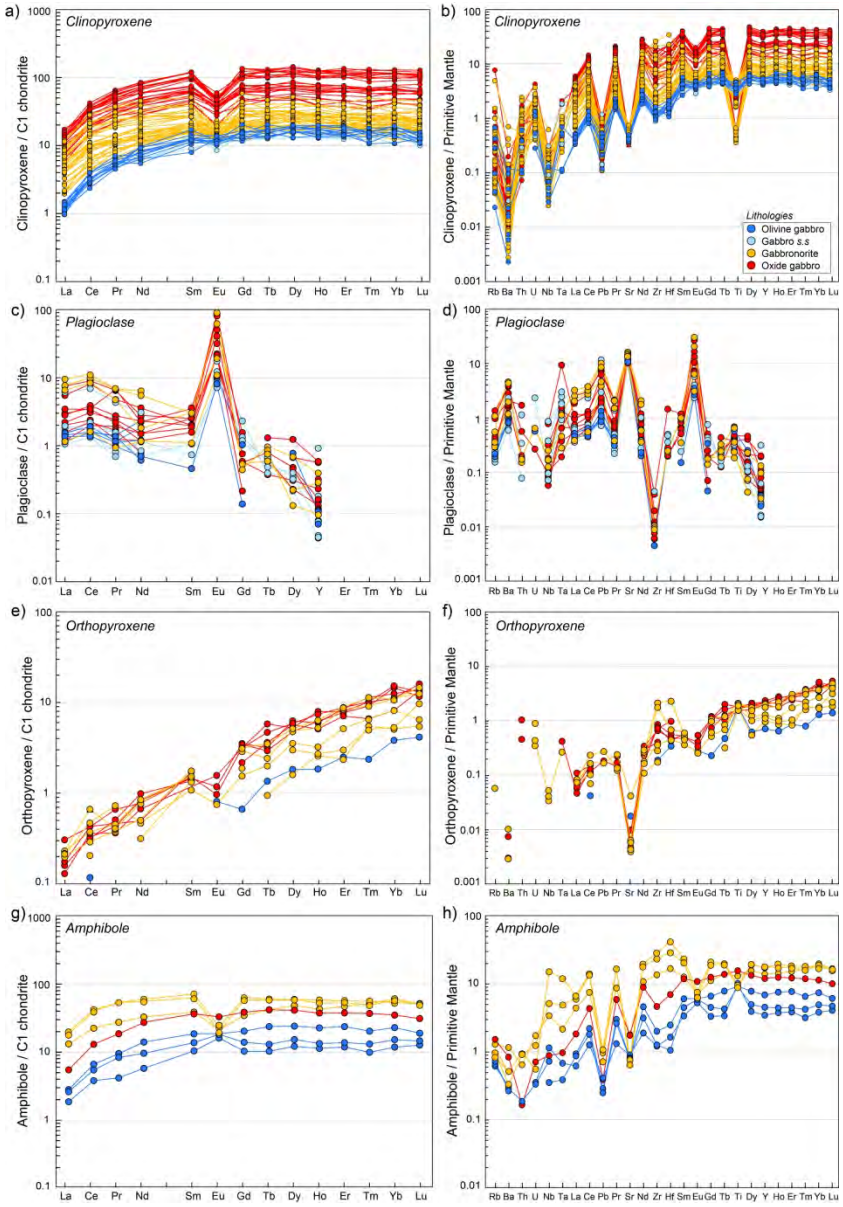

Figure 9: Mineral trace element compositions within the different gabbroic lithologies recovered in the studied area; C1-chondrite normalized REE patterns and Primitive Mantle-normalized trace element patterns of a-b) Clinopyroxene; c-d) Plagioclase; e-f) Orthopyroxene; g-h) Amphibole. Normalization values after Sun and McDonough (1989).

194x280mm (300 x 300 DPI)

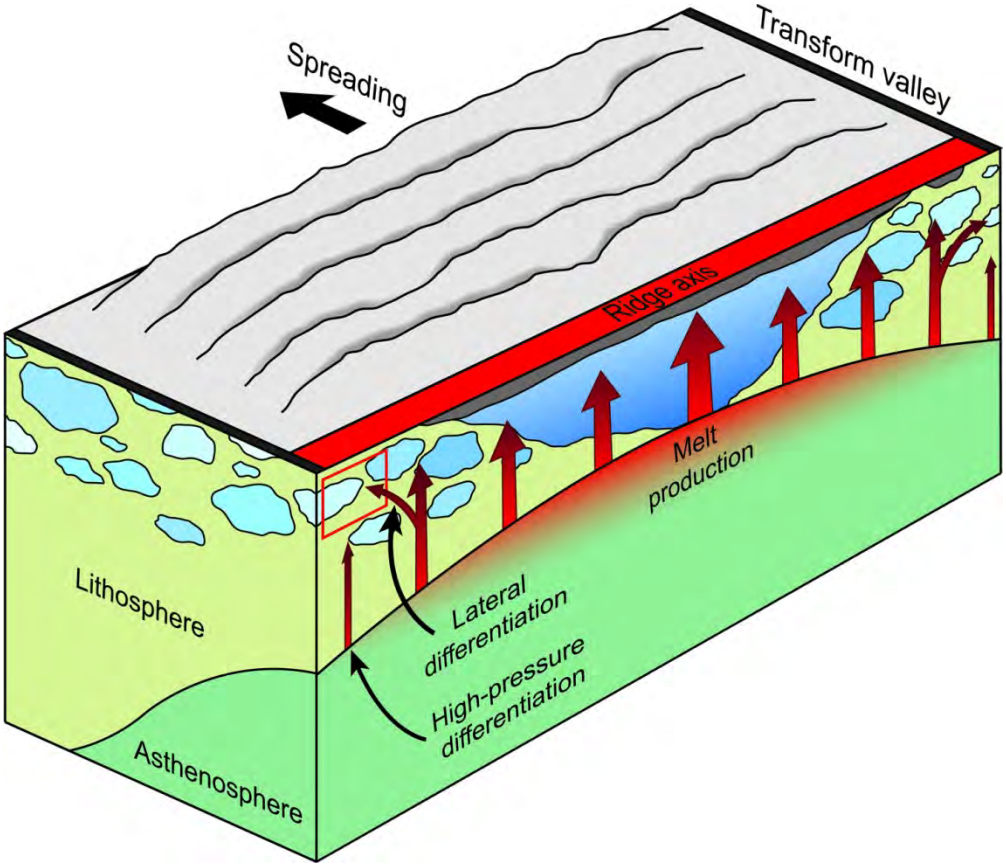

Figure 10: Representative sketch of the inferred process of lateral differentiation, resulting from the reduced melt productivity in the vicinity of the transform fault. The red box indicates the geological setting of the sketch in Figure 17.

126x108mm (300 x 300 DPI)

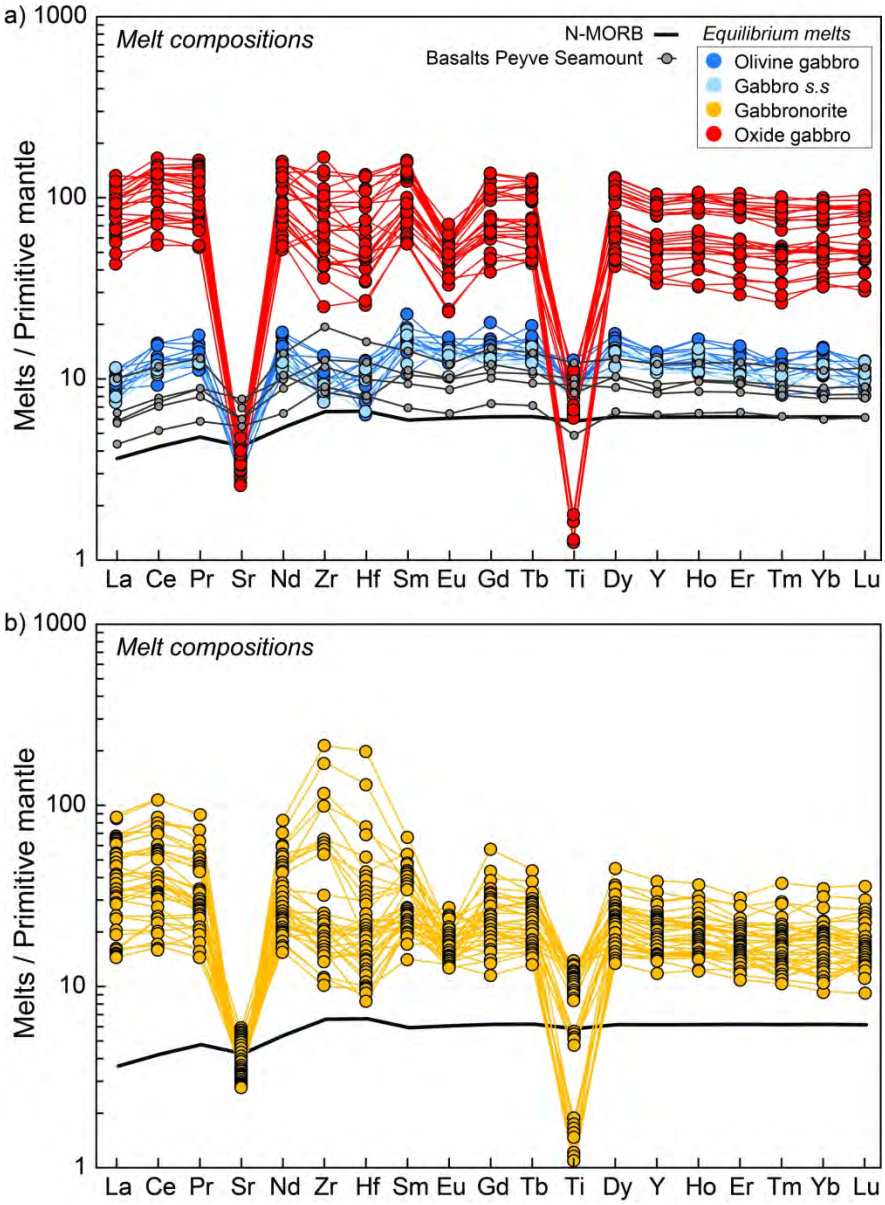

Figure 11: Primitive Mantle-normalized trace element patterns of the melts computed in equilibrium with clinopyroxene from: a) Olivine gabbros, Gabbros and Oxide gabbros; b) Gabbronorites. The trace element patterns of primitive N-MORB melts (after Workman and Hart, 2005) and the basalts sampled at the Seamount Peyve are plotted for comparison. Normalization values are after Sun and McDonough (1989) and the compilation of partition coefficients used for calculating the equilibrium melts is after Basch et al. (2018).

175x239mm (300 x 300 DPI)

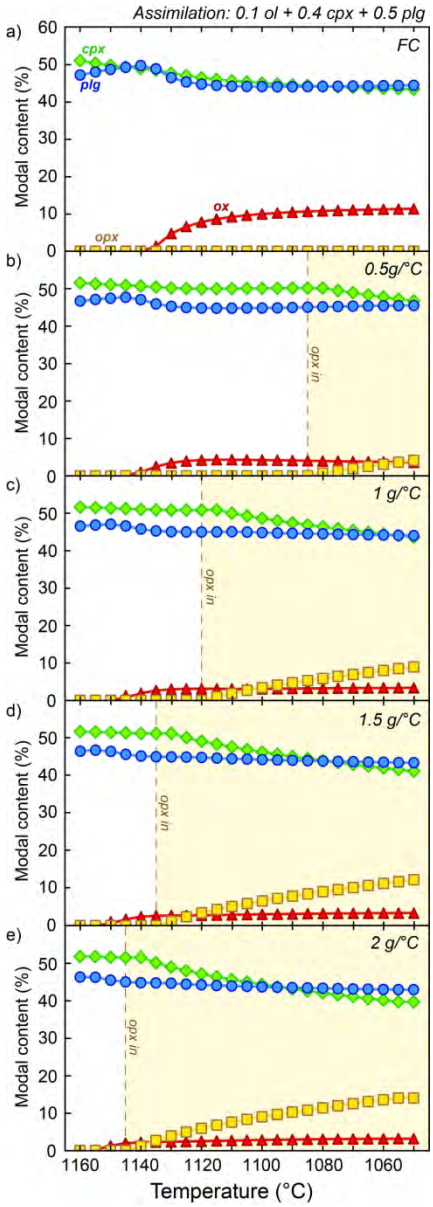

Figure 12: Modal contents (vol%) of the cumulate gabbro formed during fractional crystallization of an evolved melt, involving the assimilation of various quantities of a primitive crystal mush (10 vol% olivine, 50 vol% plagioclase, 40 vol% clinopyroxene). The composition of the basalt S45-07-173 has been selected as the starting melt composition. Models were computed using the MELTS thermodynamic software (Ghiorso and Sack, 1995). The different models assume a) Fractional Crystallization (FC); b) FC and concomitant assimilation of 0.5g/°C of cooling; c) FC and concomitant assimilation of 1g/°C of cooling; d) FC and concomitant assimilation of 1.5g/°C of cooling; e) FC and concomitant assimilation of 2g/°C of cooling. The yellow field highlights the appearance of orthopyroxene in the fractionated cumulate gabbro.

77x219mm (300 x 300 DPI)

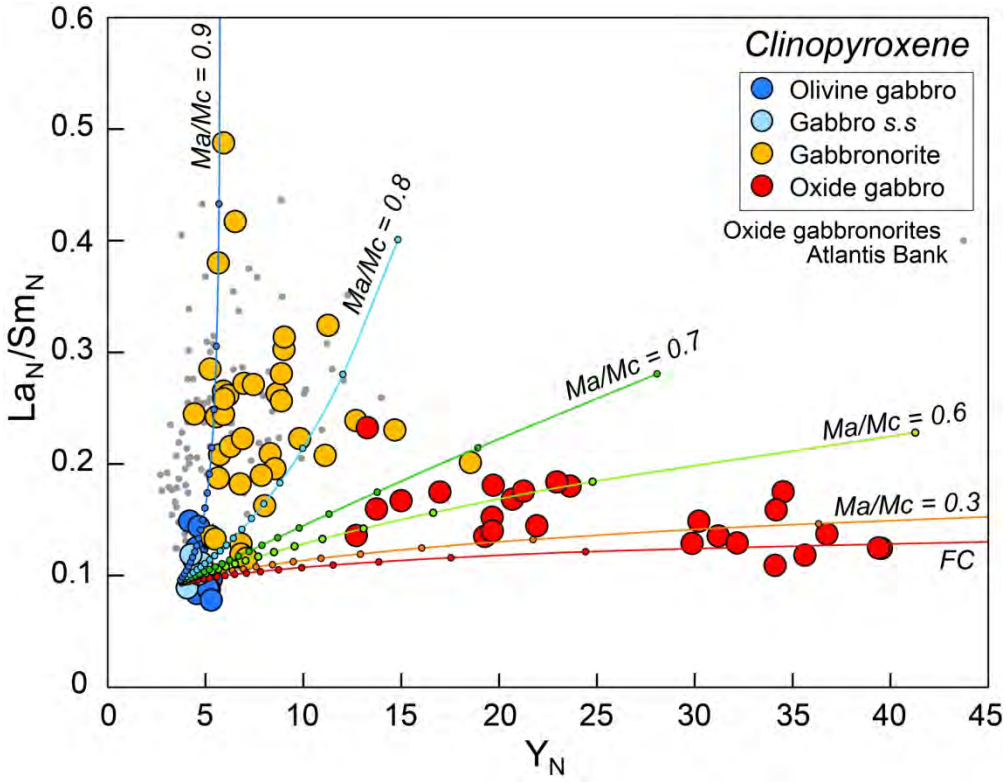

Figure 13: Clinopyroxene YN vs LaN/SmN. Compositional trends represent clinopyroxenes computed in equilibrium with melts residual after the process of Assimilation-Fractional Crystallization (AFC models, using the equation from DePaolo, 1981). Ma/Mc ranges from 0 to 0.9. Each tick along the compositional trends represents a decrease in residual melt mass of 5 vol%. Oxide gabbronorites sampled at the Atlantis Bank are shown for comparison (after Zhang et al., 2020). Normalization values are after Sun and McDonough (1989).

160x124mm (300 x 300 DPI)

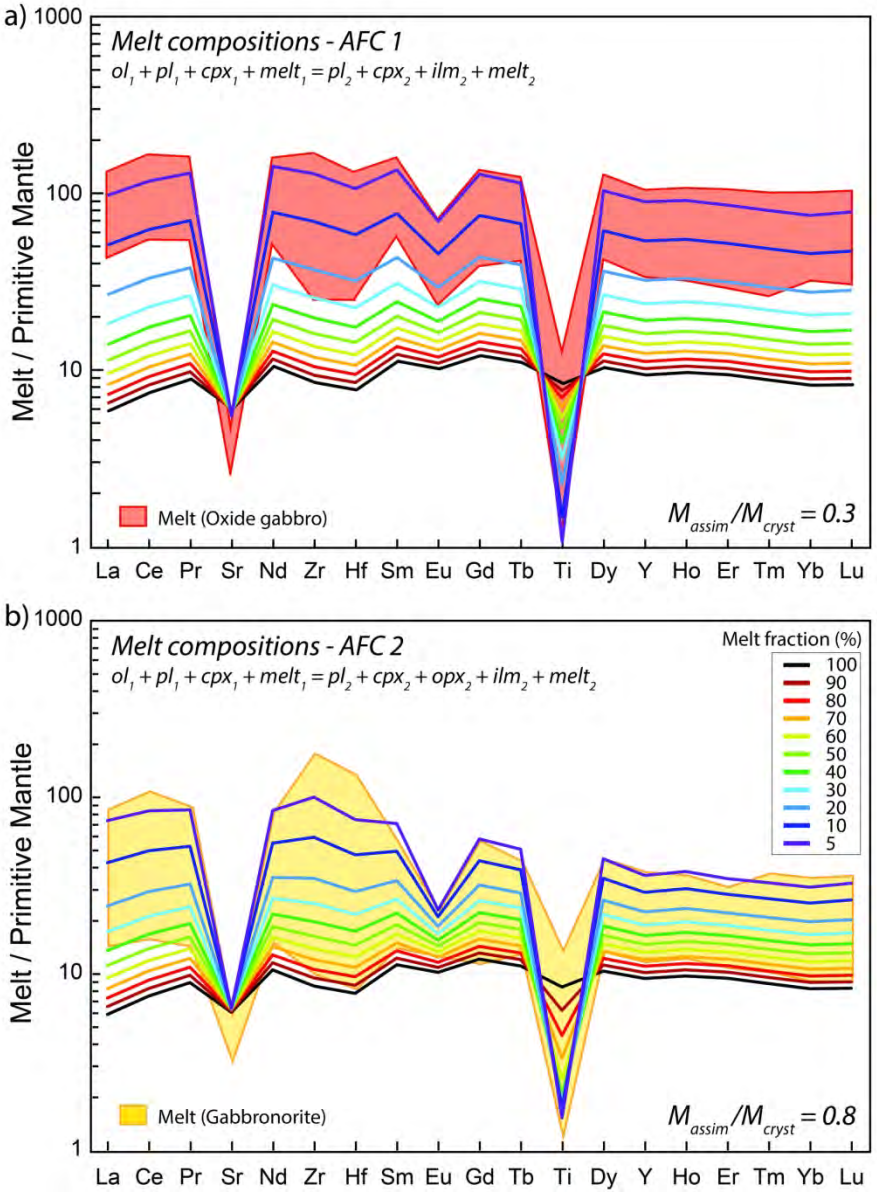

Figure 14: Primitive Mantle-normalized trace element patterns of the melt compositions in equilibrium with clinopyroxenes from Figure 13, compared with patterns of Assimilation-Fractional Crystallization (after De Paolo, 1981) of a basaltic parental composition (S45-7-180) assimilating a primitive crystal mush (10 vol% olivine, 40 vol% clinopyroxene, 50 vol% plagioclase) at variable ratios mass assimilated/mass crystallized; a) Model computed at low assimilated mass (Ma/Mc = 0.3) to reproduce the compositions of the oxide gabbros; b) Model computed at high assimilated mass (Ma/Mc = 0.8) to reproduce the compositions of the gabbronorites. Melt fraction decreases from 100% to 5% of the initial melt mass. Mineral/melt partition coefficients are after Basch et al. (2018) and normalization values are after Sun and McDonough (1989).

154x207mm (300 x 300 DPI)

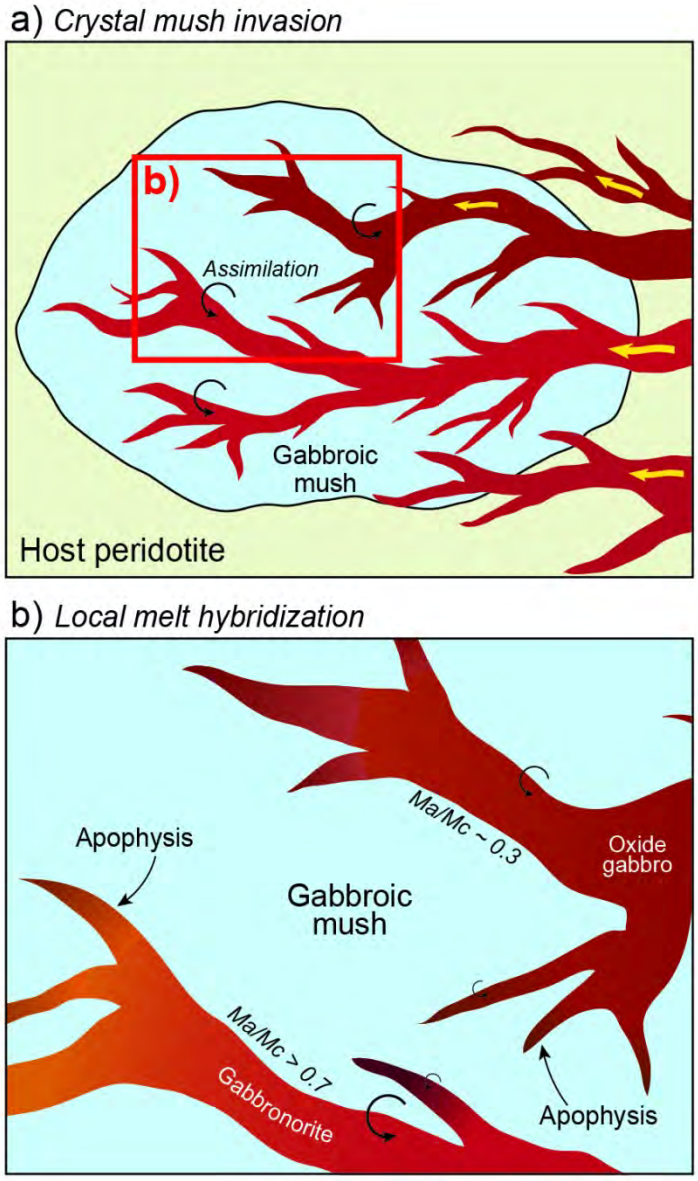

Figure 15: a) Close-up of the magmatic processes occurring in the vicinity of a cold ridge-transform intersection. A lens of primitive gabbroic crystal mush is invaded by the evolved melts percolating laterally from the central portion of the ridge segment. Reaction between the primitive crystal mush and the evolved melt leads to partial assimilation of the gabbroic mush and to the process modeled in Figures 14, 15 and 16; b) Detail of the local melt hybridization, leading to the formation of replacive lithologies ranging from oxide gabbros to oxide gabbronorites and gabbronorites. Each melt percolation channel is characterized by its intrinsic reactivity towards the primitive gabbroic mush, as a function of the melt composition and temperature. Intensive assimilation (Ma/Mc > 0.7) results in the formation of gabbronorites, whereas weaker assimilation (Ma/Mc < 0.5) leads to the formation of oxide gabbros.

76x127mm (300 x 300 DPI)